

# 1 Integer topological defects provide a new way to quantify and classify 2 cell sheets

3 Zihui Zhao<sup>1</sup>, He Li<sup>2</sup>, Yisong Yao<sup>1</sup>, Yongfeng Zhao<sup>3</sup>, Francesca Serra<sup>4,5</sup>,  
4 Kyogo Kawaguchi<sup>6,7,8,9</sup>, Hepeng Zhang<sup>1,2</sup>, Hugues Chaté<sup>10,11</sup>, and Masaki Sano<sup>1,2,6\*</sup>

5 <sup>1</sup>School of Physics and Astronomy, Shanghai Jiao Tong University, Shanghai, 200240, China.

6 <sup>2</sup>Institute of Natural Sciences, Shanghai Jiao Tong University, Shanghai, 200240, China.

7 <sup>3</sup>Center for Soft Condensed Matter Physics and Interdisciplinary Research, Soochow University,  
8 Suzhou, 215006, China.

9 <sup>4</sup>Physics and Astronomy, Johns Hopkins University, Baltimore, 21218, USA.

10 <sup>5</sup>Department of Physics, Chemistry and Pharmacy, University of Southern Denmark, Odense,  
11 113-0033, Denmark.

12 <sup>6</sup>Universal Biology Institute, The University of Tokyo, Tokyo, 113-0033, Japan.

13 <sup>7</sup>Nonequilibrium Physics of Living Matter RIKEN Hakubi Research Team, RIKEN Center for  
14 Biosystems Dynamics Research, Kobe, 650-0047, Japan.

15 <sup>8</sup>RIKEN Cluster for Pioneering Research, Kobe, 650-0047, Japan.

16 <sup>9</sup>Institute for Physics of Intelligence, The University of Tokyo, Tokyo, 113-0033, Japan.

17 <sup>10</sup>Service de Physique de l'Etat Condensé, CEA, CNRS Université Paris-Saclay, CEA-Saclay,  
18 Gif-sur-Yvette, 91191, France.

19 <sup>11</sup>Computational Science Research Center, Beijing, 100094, China.

20 \*Corresponding author(s). E-mail(s): [sano.masaki@sjtu.edu.cn](mailto:sano.masaki@sjtu.edu.cn);

## 21 Abstract

22 Sheets of confluent cells are often considered as active nematics, with accumulation at  $+\frac{1}{2}$  topological defects and  
23 escape from  $-\frac{1}{2}$  defects being widely recognized. However, collective dynamics surrounding integer-charge defects  
24 remain poorly understood, despite its biological importance. By using microfabricated patterns, we induce diverse  
25  $+1$  topological defects (aster, spirals, and target) within monolayers of neural progenitor cells. Remarkably, cells  
26 are consistently attracted to the core of  $+1$  defects regardless of their type, challenging existing theories and the  
27 conventional extensile/contractile dichotomy. We trace back the origin of this accumulation behavior to previously  
28 overlooked nonlinear active forces using a combination of experiments and a continuous theory derived from a cell-  
29 level model. Our findings demonstrate that  $+1$  topological defects can reveal key features of active nematic systems  
30 and offer a new way to characterize and classify cell layers.

## 31 1 Introduction

32 Elongated cells forming confluent layers have long been described as liquid crystal nematics, passive [1] or, more  
33 recently, active [2–6]. These active nematics display half-integer topological defects, as in the passive case, where they

34 are energetically more favorable than integer defects [7–15]. Recently gathered evidence shows that  $+\frac{1}{2}$  defects can be  
35 the location of cell accumulation or cell extrusion, whereas cell density is depleted near  $-\frac{1}{2}$  defects [16, 17]. This was in  
36 particular observed in confluent layers of Neural Progenitor Cells (NPCs). A simple hydrodynamic linear theory resting  
37 on the classic description of extensile active nematics was shown to account qualitatively for these findings [12, 16].

38 Integer topological defects are also prevalent in nature and biologically relevant, such as asters in a neural rosette,  
39 targets in plants meristem, and asters and targets during the formation of mouth, tentacles, and foot of hydra [18–22].  
40 Integer defects do not appear spontaneously in cellular nematic layers, as they tend to split into pairs of half-integer  
41 ones. However, such defects could be induced by external factors and thus also play crucial biological functions.  
42 Recently, in vitro studies have shown that +1 defects induced by strong circular confinement provide sites for growth  
43 and cellular differentiation [23]. These C2C12 myoblast cells exhibit nematic order in wider space [16]. Still, confinement  
44 leads to polar order, accumulation at defect centers and inward flow, but with a small system size and non-negligible  
45 boundary effects. Despite the biological importance of morphogenesis, we still lack quantitative measurements of  
46 tissue properties and large-scale flow dynamics of active nematics within stable and well-defined topological defect  
47 configurations.

48 In dense conditions, NPCs take elongated shapes and display stochastic back-and-forth motion without apparent  
49 contact inhibition or strong cell-cell adhesion [16], exhibiting local nematic order. These characteristics make NPCs an  
50 excellent system for building hierarchical descriptions of active nematics, from the individual cell level to continuous  
51 theory, a rare feat we take advantage of here.

52 To investigate the behavior of cellular active nematics with integer defects, we induce +1 defects in NPC layers by  
53 letting cells proliferate on patterned substrates. We consider a one-parameter family of +1 defects from aster to target  
54 via spiral vortices and show that cells accumulate at their center in all cases, suggesting potential biological importance.  
55 A similar effect was recently observed with fibroblasts proliferating on a target pattern [24, 25], and attributed to a  
56 higher cell division rate at the defect core rather than to the large-scale motion of cells typical of hydrodynamic theories  
57 [25]. In contrast, we demonstrate here that our system does exhibit large-scale inward cellular flows. We further show  
58 that our findings cannot be explained by the simple hydrodynamic theory used in the unpatterned ‘natural’ case,  
59 since this theory predicts outward flows for the target. We perform a complete modeling of our system, starting from  
60 a minimal particle/cell level model incorporating its basic features, deriving a nonlinear hydrodynamic theory from it,  
61 and analyzing its solutions. Details of this modeling program will appear elsewhere [26]. Analysis of the experiment,  
62 based on this theory, reveals that nonlinear active force terms neglected in simpler approaches play a crucial part  
63 in explaining cellular flows around defects. We estimate all the coefficients that characterize the theory. Our results  
64 suggest a new classification of active nematics and reveal important physical mechanisms heretofore ignored, which  
65 are likely to play a role in various contexts given the genericity of our approach.

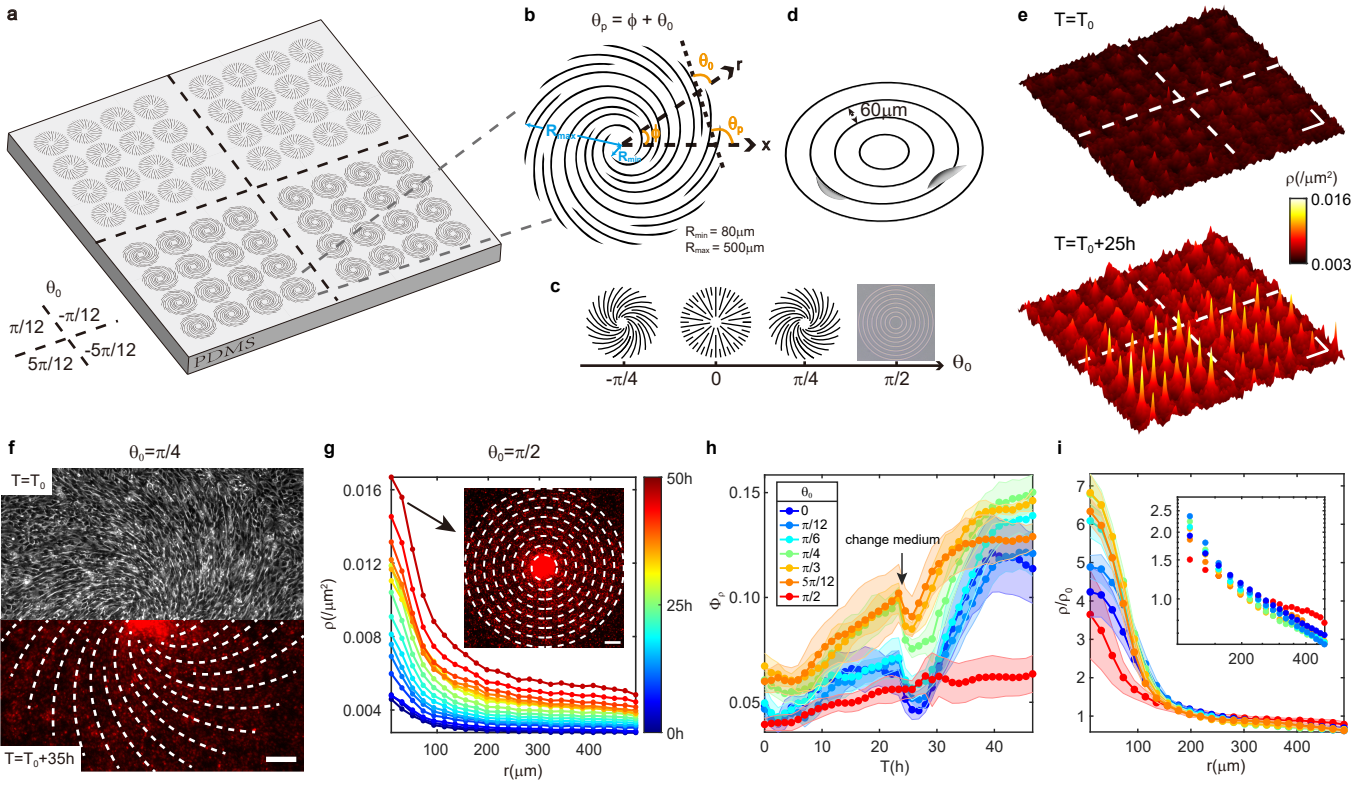


**Fig. 1** NPCs accumulate at centers of asters, spirals, and targets. **a**, Schematic of microfabricated patterns on a PDMS substrate. Four arrays of different spirals ( $\theta_0 = \pm\pi/12, \pm 5\pi/12$ ) are arranged on one PDMS sheet, featuring 16 micropatterns per defect type. **b**, Schematic of +1 topological defect definition. The largest radius of patterns ( $R_{max}$ ) is  $500\mu\text{m}$ . The radius of the defect center without ridges ( $R_{min}$ ) is  $80\mu\text{m}$ . The distance between ridges is in the range of  $30 - 120\mu\text{m}$ . **c**, Types of +1 topological defects characterized by the tilt angle  $\theta_0$ . A bright-field image is shown for targets. **d**, Schematic of cell motion on a target pattern. **e**, Heatmap of cell density at the beginning and after 25 hours of recording on spirals shown in **a**.  $T = T_0$  at the onset of confluence. **f**, A typical phase-contrast image at the beginning and a typical fluorescent image after 35 hours of recording on a spiral with  $\theta_0 = \pi/4$ . Dashed lines depict ridges of patterns. **g**, Time evolution of average radial density profiles on the target. The data was averaged every one hour and by 32 targets. Inset: a typical fluorescent image showing accumulation after 50 hours of recording on a target. Dashed lines depict ridges. **h**, Average percentage of cells  $\Phi_r$  ( $\Phi_r = n(r < R_{min})/n(r < R_{max})$ , where  $n$  is the cell number) assemblies over time on aster, counterclockwise spirals and target. Colors depict different defects. The number ( $N$ ) of each type of defect is 6 and all defects was designed on one PDMS sheet. **i**, Normalized radial density profiles by mean density  $\rho_0$  when  $\rho_0 = 0.009/\mu\text{m}^2$ . Inset: A log-log plot for the region with  $r > 100\mu\text{m}$ .  $N$  of aster, each type of spiral, target is 32, 6 and 32. Legend in **h**. In **h** and **i**, data are presented as mean  $\pm$  s.d., and s.d. are calculated from defects in an array. Scale bars,  $100\mu\text{m}$ .

## 66 2 Results

### 67 2.1 NPCs accumulate at the center of +1 topological defects

68 To investigate the effect of +1 topological defects on cell monolayers, we cultured NPCs on microfabricated poly-  
 69 dimethylsiloxane (PDMS) patterns featuring various defect types delineated by  $1.2\mu\text{m}$ -high ridges (Fig. 1a, Methods).  
 70 These patterns are defined by their tilt angle  $\theta_0$ : everywhere in space, but here only along the fabricated shallow  
 71 ridges,  $\theta_p = \phi + \theta_0$ , where  $\theta_p$  is the preset local orientation,  $\phi$  is the polar angle, and  $\theta_0$  ( $\theta_0 \in (-\pi/2, \pi/2]$ ) is the  
 72 tilt angle relative to the radial direction (Fig. 1b) [27]. Specific values  $\theta_0 = 0, \pm\pi/12, \pm\pi/6, \pm\pi/4, \pm\pi/3, \pm 5\pi/12, \pi/2$   
 73 were used. Note that  $\theta_0 = 0, 0 < \theta_0 < \pi/2, -\pi/2 < \theta_0 < 0, \theta_0 = \pi/2$ , correspond to aster, counterclockwise spirals,  
 74 clockwise spirals and target respectively (Fig. 1c). The patterns had a maximal radius  $R_{max} = 500\mu\text{m}$ , and included a  
 75 central ridge-less area with a radius  $R_{min} = 80\mu\text{m}$ . The shallow ridges can be considered to constitute weak external

76 fields since the cells retained their ability to easily climb and cross over them (Fig. 1d, Supplementary Video 1). They  
77 gently guided cells and led to the emergence of +1 defects in the confluent cell monolayer (Fig. 1f).

78 We conducted long time-lapse recordings after confluence and observed that cells gradually accumulated over time  
79 at the centers of defects irrespective of  $\theta_0$  (Fig. 1e,f,g, Methods). The local cell density  $\rho$  was measured from nuclear  
80 fluorescence intensity (Methods). Averaging the configurations azimuthally, we obtained the time-evolution of cell  
81 density radial profiles across all patterns (Fig. 1g, Extended Data Fig. 1a,2a). The ratio  $\Phi_\rho$ , representing the number  
82 of cells within the radius  $R_{min}$  around defect center relative to the total number, exhibits a continuous increase except  
83 during periods of medium changes (Fig. 1h, Extended Data Fig. 1b,2b, Supplementary Video 2) [28]. Radius-dependent  
84 average cell densities on different defects with the same total density display distinct accumulation around centers  
85 and similar slopes in log-log plot in the regions other than centers (Fig. 1i, Extended Data Fig. 1c). Additionally,  
86 the accumulation behavior is more prominent on counterclockwise patterns, potentially attributable to NPCs' weak  
87 chirality (Extended Data Fig. 2b,2c) [29].

## 88 2.2 Orientation and dynamics of NPCs in induced topological defects

89 When forming a confluent monolayer, cells demonstrated a tendency to align with their neighbors and with the guiding  
90 patterns (Fig. 2a-c). The local orientation of this nematic order hardly changed throughout the recording. Applying the  
91 structure tensor method to phase-contrast images and averaging orientations locally over space and time, we obtained  
92 local nematic orientation fields (Fig. 2a-c, Extended Data Fig. 3a, Methods). To quantify the degree of orientational  
93 order, we calculated the local scalar order parameter  $S$ .  $S$  is minimal at the center, increases with radius, and slightly  
94 decreases near the edges due to the looser confinements (Fig. 2d, Extended Data Fig. 3d). However accurate orientation  
95 measurements were hindered around defect centers due to the presence of high densities and three-dimensional cell  
96 mounds in these areas. Coherency analysis also indicates that the estimated orientations are more reliable in outer  
97 regions than around centers. (Extended Data Fig. 3e,f, Methods).

98 To evaluate the impact of guiding ridges, we measured the angle  $\Delta\theta$  between local cell orientation ( $\theta$ ) and the  
99 preset pattern orientation ( $\theta_p$ ). We found that  $\Delta\theta$  does not change much over radius (Fig. 2e, Extended Data Fig.  
100 3g). To avoid inaccuracies, we did global average in regions with  $r > 100\mu m$  and consistently observed that  $\Delta\theta$  was  
101 around  $-4^\circ$  across all defects, indicating a weak clockwise chirality (Fig. 2f). Comparable results were obtained from  
102 orientational fields extracted from the long axis of nuclei (Fig. 2f, Extended Data Fig. 3b,c, Methods). This observation  
103 of the small value validates the successful induction of the designed defects in the cell monolayer.

104 To investigate whether the aggregation in defect central areas is related to collective movements, we conducted  
105 a quantitative analysis of cell dynamics. Trajectories depicted in (Fig. 3a-b) were extracted by tracking cell nuclei  
106 (Methods, Supplementary Video 3-6). Individual cells exhibit bidirectional motion with an instantaneous speed around  
107  $0.4\mu m/min$  and a typical reversal time of 1-2 hours (Fig. 3c, Methods). By coarse-graining instantaneous velocities  
108 during the continuous accumulation periods (10 hours) in Fig. 1h, we obtained spatiotemporally averaged net velocity

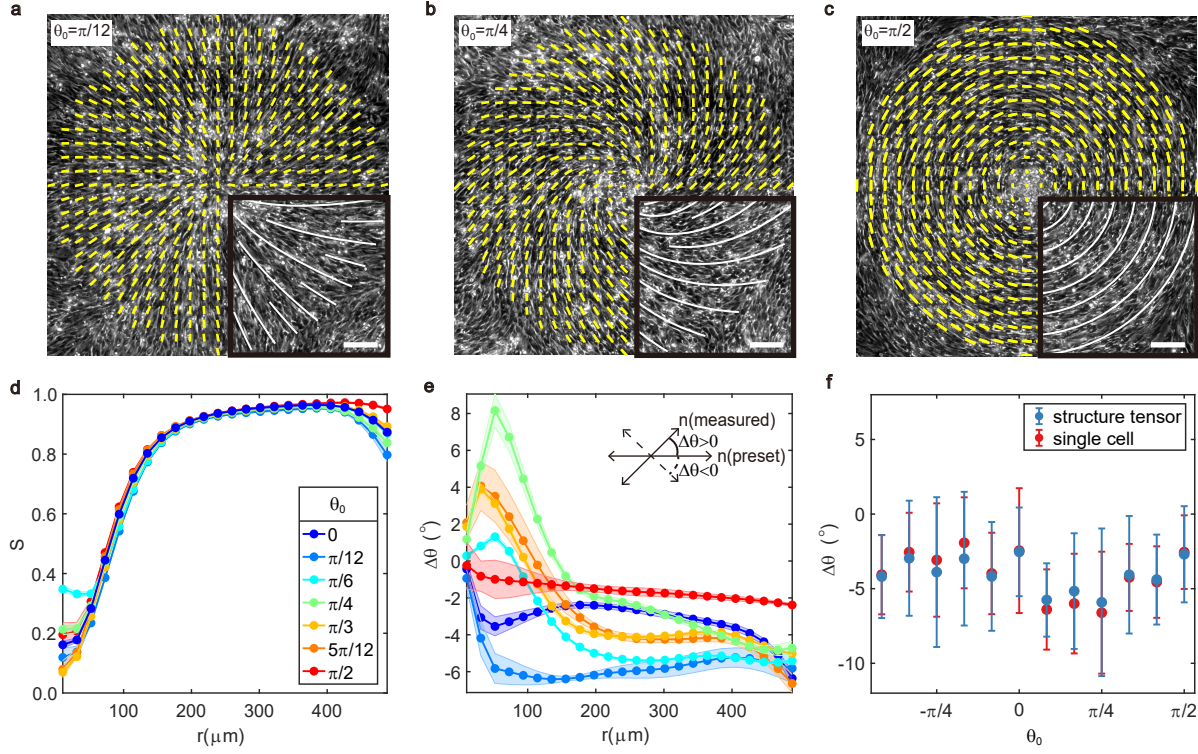


**Fig. 2** Cellular orientation around induced  $+1$  defects. **a, b, c**, Spatiotemporally averaged orientational fields on defect pattern with  $\theta_0 = \pi/12, \pi/4, \pi/2$ , respectively. Yellow lines depict local nematic orientation, with their length corresponding to local coherency. Background: phase-contrast images, from which we can observe cell bodies. Insets: white lines show the shallow ridges defining patterns. **d**, Radial profiles of order parameter  $S$  on aster, counterclockwise spirals and target. **e**, Same as **d** but for the angle  $\Delta\theta$  between the experimentally measured cell orientation and orientation preset by PDMS pattern. Preset orientation refer to cellular alignment if cells form perfect topological defects according to definition. Inset shows the definition of  $\Delta\theta$ :  $\Delta\theta > 0$  when the measured orientation (measured  $\mathbf{n} = (\cos \theta, \sin \theta)$ ) rotates counterclockwise against the preset orientation (preset  $\mathbf{n}_p = (\cos \theta_p, \sin \theta_p)$ ), vice versa  $\Delta\theta < 0$ . **f**,  $\Delta\theta$  across all types of defects. In **a-f**, data are averaged by 32 asters (10h), 16 spirals for each type (10h) and 32 targets (10h). In **d-e**, data are presented as mean  $\pm$  s.d., and s.d. are calculated from different times. In **f**, data are presented as mean  $\pm$  s.d., and s.d. are calculated from different positions of average orientational fields (regions with  $r < 100\mu\text{m}$  are excluded). Scale bars,  $100\mu\text{m}$ .

fields (Extended Data Fig. 4a, Methods, see Supplementary Video 3-6 for time evolution of spatially averaged net velocity fields). Streamlines calculated from these net velocity fields demonstrate the inward direction of cellular flows (Fig. 3d-f). Notably, the local velocities are typically not aligned with the local orientation. Averaging radial net velocities along the azimuthal direction shows inward net radial velocities across all defects (Fig. 3g, Extended Data Fig. 4b), consistent with observed cell accumulation around defect cores. In our measurements here and subsequent fitting process, we focused on a timescale of 10 hours, during which cells did not proliferate much since cell division typically occurs over approximately 24 hours [16].

We further analyzed the probability distribution function of angles ( $\theta_v$ ) between net velocities and inward radial directions. To avoid inaccuracies of tracking single cells in high-density centers, we excluded the regions with  $r < 100\mu\text{m}$ . These angles ( $\theta_v$ ) are predominantly situated in the inward region ( $-90^\circ < \theta_v < 90^\circ$ ) (Fig. 3h). After extracting the peak location of  $\theta_v$  for each defect in (Fig. 3h) and incorporating the deviations  $\Delta\theta$  in (Fig. 2f) into preset  $\theta_0$  ( $\theta_0(measured) = \theta_0 + \Delta\theta$ ), we finally delineated how  $\theta_v$  changes with measured  $\theta_0$  (Fig. 3i). Comparable

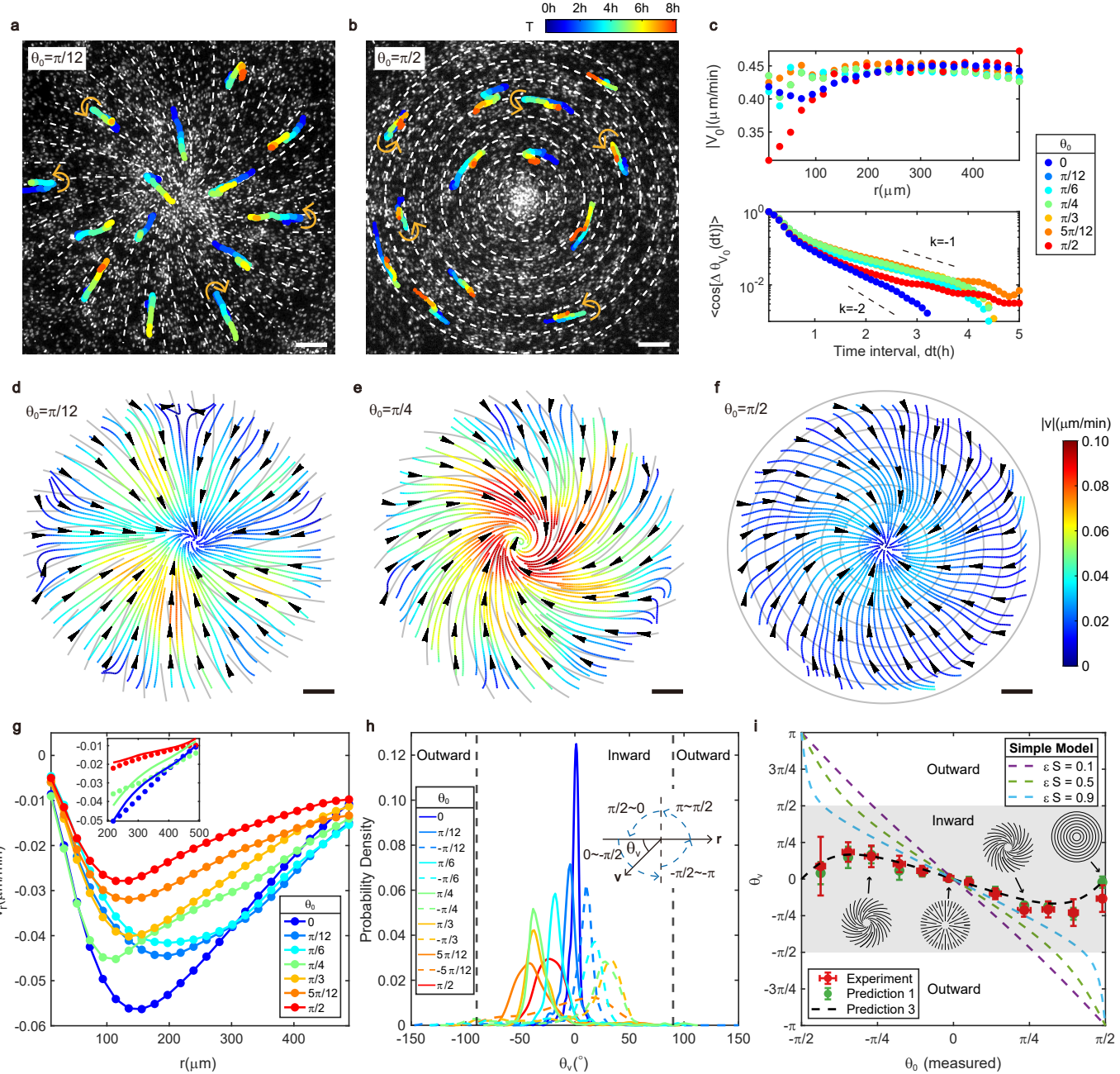


**Fig. 3** Cellular dynamics during accumulation toward +1 defect cores. **a, b**, Bidirectional motion of single NPC on defects with  $\theta_0 = \pi/12, \pi/2$ , respectively. Trajectories are traveled in time as indicated by color. Color bar in **b**. Background: fluorescent images, from which we can observe cell nuclei. Dashed lines indicate the guiding ridges of patterns. **c**, Radial profiles of the amplitude of average instantaneous velocity  $V_0$  when mean density is around  $0.005/\mu\text{m}^2$  (upper) and autocorrelation of the direction ( $\theta_{V_0}$ ) of instantaneous velocity as a function of time interval  $dt$  (lower).  $k = -1$  ( $k = -2$ ) corresponds to 2 hours' (1 hour's) reversal time. **d, e, f**, Streamlines on defects with  $\theta_0 = \pi/12, \pi/4, \pi/2$ , respectively. Gray lines indicate guiding ridges. Color represents the amplitude of net velocities. Color bar in **f**. **g**, Radial profiles of the average radial net velocity ( $V_r$ ) components on aster, counterclockwise spirals and target. Inset: Comparison between experimentally measured radial velocity profile (dots) and predictions (lines) at large  $r$  on the aster, spiral ( $\theta_0 = \pi/4$ ) and target. The prediction comes from method (ii). **h**, Probability density function of the angle ( $\theta_v$ ) between net velocity and inward radial direction on all types of defects. Insets show the definition of  $\theta_v$ . **i**, Measured and predicted  $\theta_v$  versus measured  $\theta_0$ .  $\theta_0(\text{measured}) = \theta_0 + \Delta\theta$ . Prediction 1 (3) comes from method (i) ((iii)). Data are presented as mean  $\pm$  s.d. in horizontal axis and the location of peak  $\pm$  FWHM of PDF shown in **h** in vertical axis. FWHM and s.d. are calculated from different positions of average net velocity fields (regions with  $r < 100\mu\text{m}$  are excluded). In **c – i**, data are averaged by 32 asters (10h), 16 spirals for each type (10h) and 32 targets (10h). Scale bars,  $100\mu\text{m}$ .

121 results were obtained with optical flow method (Extended Data Fig. 4c,d, Methods). Symmetry-breaking shown in  
 122 Fig. 2f, Fig. 3f, Fig. 3h indicates the presence of chirality.

123 **2.3 Detecting the relation between net cellular flows and active forces**

124 Conventional active nematic theories typically include an equation relating a velocity field to an active force term:

125 
$$\gamma \mathbf{v} = -\zeta \nabla \cdot \mathbf{Q} \quad (1)$$

126 where  $\gamma$  is friction coefficient, and  $\mathbf{Q} = S \begin{pmatrix} \cos(2\theta) & \sin(2\theta) \\ \sin(2\theta) & -\cos(2\theta) \end{pmatrix}$  is the nematic order parameter tensor with  $\theta$  being the  
 127 local cell orientation. The active force ( $\mathbf{f}$ ) can formally be identified as the divergence of active stress  $-\zeta \mathbf{Q}$ , leading  
 128 to  $\mathbf{f} = -\zeta \nabla \cdot \mathbf{Q}$  [30, 31]. In the ‘unpatterned’ natural state,  $+ \frac{1}{2}$  defects in the confluent NPCs are observed to move  
 129 in the ‘head’ direction [16, 32], considered as a characteristic of an extensile system with  $\zeta > 0$ .

130 In our experiments, cells aligned well with the guiding patterns, resulting in a significantly slower timescale for  
 131  $\mathbf{Q}$  dynamics compared to accumulation processes. Therefore, we assume  $\mathbf{Q}$  is fixed in time by the ‘external field’  
 132 induced by the pattern. For  $+1$  defects with  $\theta = \theta_p = \phi + \theta_0$ , the linear active force field becomes  $\mathbf{f} = -\zeta [S'(r) +$   
 133  $\frac{2S(r)}{r}] (\cos 2\theta_0 \hat{\mathbf{r}} + \sin 2\theta_0 \hat{\phi})$ , where  $S'(r) = \frac{dS(r)}{dr}$ ,  $\hat{\mathbf{r}}$  ( $\hat{\phi}$ ) is the unit vector in the radial (azimuthal) direction. In a  
 134 uniform and confluent state where  $S'(r) > 0$  near the center, the radial component is inward for  $0 \leq |\theta_0| < \pi/4$  but  
 135 outward for  $\pi/4 < |\theta_0| \leq \pi/2$ , indicating possible outward flows for large  $|\theta_0|$  (Fig. 4a). This is at odds with the inward  
 136 flows observed with all types of induced  $+1$  defects. In particular, this suggests that within this simple theory, the  
 137 collective behavior around large  $|\theta_0|$  defects like targets is that of a contractile system ( $\zeta < 0$ ).

138 The linear theory can be refined by considering an anisotropic friction  $\gamma = \gamma_0(I - \epsilon \mathbf{Q})$ , with the anisotropy coefficient  
 139  $0 \leq \epsilon \leq 1$  describing larger friction along the direction perpendicular to cell alignment [12, 16]. However, comparing  
 140 measured  $\theta_v$  with predicted  $\theta_v$  from this extended simple theory shows that this fails to explain cell accumulation and  
 141 inward flows for all defects types (Fig. 3i).

142 To understand the underlying mechanisms driving inward cellular flows, we performed a complete modeling of our  
 143 system, starting from a minimal particle/cell level dry active nematic model where the induced patterns are accounted  
 144 for by some external field. Numerical simulations of this model showed particle accumulation irrespective of the type  
 145 of  $+1$  defect, in broad agreement with our experimental results. Confident in the faithfulness of this model, we derived  
 146 from it a nonlinear hydrodynamic theory using a Boltzmann-Ginzburg-Landau approach (Supplementary Information:  
 147 Section 4) [26, 33–35]. The theory shows the presence of two ‘nonlinear active force terms’ in addition to the standard  
 148 active force. Incorporating these terms and accounting for spatial density variations, the total active force replacing  $\mathbf{f}$   
 149 is

150 
$$\mathbf{f}^a = -\zeta \nabla \cdot \rho \mathbf{Q} + \gamma_2 \rho \mathbf{Q} \cdot (\nabla \cdot \rho \mathbf{Q}) + \gamma_1 (\rho \mathbf{Q} \cdot \nabla) \cdot \rho \mathbf{Q}. \quad (2)$$

151 In the steady state with ideal orientations,  $\theta = \theta_p = \phi + \theta_0$ , equation (2) can be written in polar coordinates as

152 
$$\mathbf{f}_r^a = \left[ (\rho S(r))' + 2 \frac{\rho S(r)}{r} \right] (-\zeta \cos 2\theta_0 + \gamma_2 \rho S(r)) + \left[ (\rho S(r))' - 2 \frac{\rho S(r)}{r} \right] \gamma_1 \rho S(r). \quad (3)$$

153 
$$\mathbf{f}_\phi^a = - \left[ (\rho S(r))' + 2 \frac{\rho S(r)}{r} \right] \zeta \sin 2\theta_0, \quad (4)$$

154 where  $(\rho S(r))' = \frac{d(\rho(r)S(r))}{dr}$ . Our derivation shows that  $\gamma_2 < 0$  and that  $\gamma_1 > 0$  generally holds in most cases  
 155 (Supplementary Information: Section 4). Therefore, the two nonlinear active forces point towards the defect cores,  
 156 which contributes to inward flows and central cell accumulation (Fig. 4a) (Note that a  $\mathbf{Q} \cdot (\nabla \cdot \mathbf{Q})$  term was considered  
 157 in [36] in the context of active suspensions, where it was shown to be able to stabilize nematic order). Our theory  
 158 taking into account variations of the cell density  $\rho$ , the net velocity of cellular flow is governed by

159 
$$\Gamma \rho \mathbf{v} = \mathbf{f}^a - \pi_0 \nabla \rho, \quad (5)$$

160 where  $\Gamma = \gamma_0(I - \epsilon \rho \mathbf{Q})$ ,  $0 \leq \epsilon \rho \leq 1$  and  $\pi_0 > 0$ .

161 To test the relation between cellular flow and active forces from experimental data, we decomposed them into the  
 162 parallel and perpendicular components relative to the principal axis of local  $\mathbf{Q}$  in regions outside centers (Extended  
 163 Data Fig. 5). In Fig. 4b-d, we present parallel components on asters and spirals ( $\theta_0 = \pi/4$ ) and perpendicular  
 164 components on targets and spirals ( $\theta_0 = \pi/4$ ) as they represent the primary components associated with inward flows  
 165 on corresponding patterns. Concerning the  $\nabla \cdot \rho \mathbf{Q}$  term, the parallel components exhibit negative correlations with the  
 166 net velocity, while perpendicular components show positive ones (Fig. 4b), another indication that the simple theory  
 167 cannot fully explain the observed phenomena. However, for  $\rho \mathbf{Q} \cdot (\nabla \cdot \rho \mathbf{Q})$  and  $(\rho \mathbf{Q} \cdot \nabla) \cdot \rho \mathbf{Q}$  terms, these components show  
 168 consistent negative (Fig. 4c) and consistent positive correlations (Fig. 4d) respectively. These comparisons provide  
 169 evidence for the relevance of the two nonlinear active forces.

170 **2.4 Predicting cellular flows from local orientations**

171 From experimental data, we extracted the value of each term in equations (2,5) using the average net velocities,  
 172 orientations, and densities outside the centers. To quantitatively assess our theory, we of course also need to estimate  
 173 their coefficients. We identified the best-fit values by Bayesian inference. During fitting, we replaced  $\rho$  in equations  
 174 (2,5) with the normalized density  $\rho/\rho_0$ , where  $\rho_0$  is the mean density. The fits yielded values for five model parameters:  
 175  $\epsilon' = \rho_0 \epsilon$ ,  $\zeta' = \zeta/\gamma_0$ ,  $\gamma_2' = \gamma_2 \rho_0/\gamma_0$ ,  $\gamma_1' = \gamma_1 \rho_0/\gamma_0$ ,  $\pi_0' = \pi_0/\gamma_0$ . For each defect type, we determined the best-fit  
 176 values (Extended Data Tab. 1). We then averaged these best-fit values over the different defect types and found:  
 177  $\epsilon' = 0.1476 \pm 0.0876$ ,  $\zeta' = 0.0289 \pm 0.0131(\mu\text{m}^2/\text{s})$ ,  $\gamma_2' = -0.0257 \pm 0.0153(\mu\text{m}^2/\text{s})$ ,  $\gamma_1' = 0.0564 \pm 0.0144(\mu\text{m}^2/\text{s})$ ,  $\pi_0' =$   
 178  $0.0732 \pm 0.0294(\mu\text{m}^2/\text{s})$ , with standard deviations as errors. It is worth noting that since not all experiments were  
 179 conducted simultaneously, standard deviations may be large due to varying cell conditions. However, the signs  $\zeta' >$   
 180  $0$ ,  $\gamma_2' < 0$ ,  $\gamma_1' > 0$  are maintained and the order of magnitude of the coefficients is found steady.

181 We conducted three distinct approaches to predict cellular flows from equation (5). (i) Utilize the measured  $\mathbf{Q}$  and  
 182  $\rho$  fields from experiments for each defect type with best-fit parameters; (ii) Employ the same fields but use average

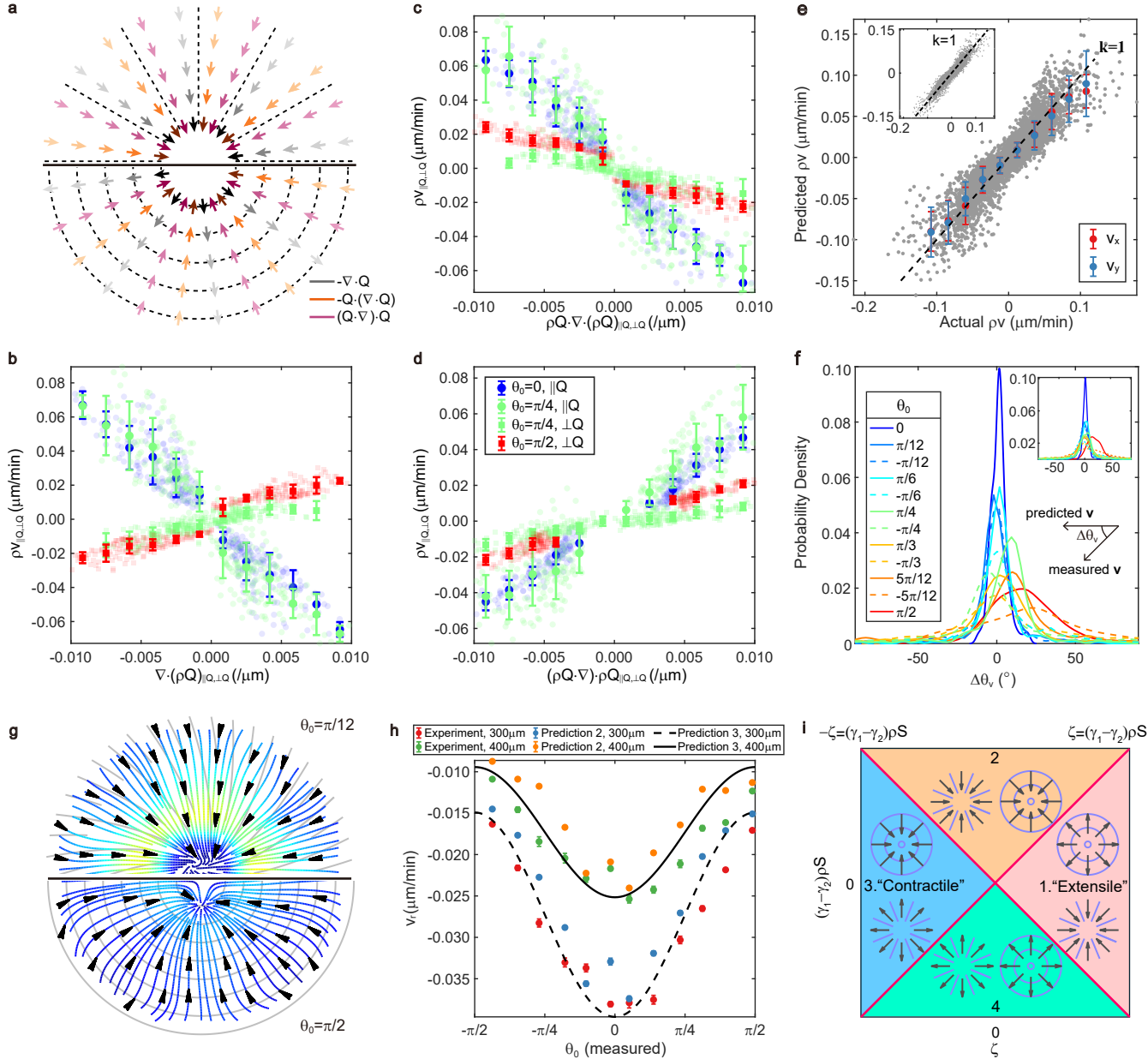


**Fig. 4** Prediction of cellular flows from active forces. **a**, Schematic of active forces on aster and target when  $S$  is a constant. Darker color means stronger force. **b, c, d**, Comparisons between components of cellular flow  $\rho v$  and components of active forces  $\nabla \cdot (\rho \mathbf{Q})$  (**b**),  $\rho \mathbf{Q} \cdot (\nabla \cdot \rho \mathbf{Q})$  (**c**),  $(\rho \mathbf{Q} \cdot \nabla) \cdot \rho \mathbf{Q}$  (**d**).  $\rho v_{\parallel \mathbf{Q}}$  ( $\rho v_{\perp \mathbf{Q}}$ ) is defined as the flow component parallel (perpendicular) to the principal axis of  $\mathbf{Q}$ , so as for components of active forces. Comparisons between parallel components are plotted for the aster and spiral ( $\theta_0 = \pi/4$ ); Comparisons between perpendicular components are plotted for the target and spiral ( $\theta_0 = \pi/4$ ). Error bars are s.d. **e**, Comparison between experimentally measured cellular flows and predictions. Determinate coefficient  $R^2 = 0.8173$ . The scatter plot denotes raw data (gray) on all the patterns (regions with  $r < 100\mu\text{m}$  are excluded). Symbols show the average values of predictions. The prediction method is method (ii). Error bars are s.d. Insets show results from prediction method (i). In **b** – **e**,  $\rho$  is normalized by mean density. **f**, Probability density function of the angle ( $\Delta\theta_v$ ) between experimentally measured net velocities and predicted net velocities. The prediction method is method (ii). Insets show the definition of  $\Delta\theta_v$  and results from prediction method (i). **g**, Predicted streamlines on the spiral ( $\theta_0 = \pi/12$ ) and target. Color bar in Fig. 3f. The prediction method is method (i). **h**, Comparison between measured net radial velocity and predictions at  $r = 300\mu\text{m}$  and  $r = 400\mu\text{m}$  of all the defects. Method of prediction 2 (3) is method (ii) ((iii)). Data are presented as mean  $\pm$  s.e.m. **i**, New classification of active nematics. The functions defining two red lines are shown on the top left and top right.

parameters; (iii) Generate an  $S(r)$  profile and a  $\rho(r)$  profile by averaging across all defects, use average parameters and active force components in equations (3,4). By comparing the amplitudes and angles of measured and predicted net velocities, we discovered that while the best-fit parameters yielded the most accurate predictions, the average

parameters also provided acceptable predictions (Fig. 4e,f). Through methods (i) and (ii), we obtained predicted velocity fields for all defects (Extended Data Fig. 6a,7a) and displayed streamlines on a spiral and target (Fig. 4g). In Extended Data Fig. 8 and Fig. 3g, we compared the predicted and measured net radial and azimuthal velocity profiles. Further, outside the centers, where density profiles of all defect types are similar, the measured and predicted net radial velocities exhibit the same cosine-like tendency over  $\theta_0$  (Fig. 4h), consistent with the radial components of active forces in the equation (3). Moreover, the predicted tendency of  $\theta_v$  over  $\theta_0$  closely matched the measured tendency, contrasting sharply with the simple theory (Fig. 3i, Extended Data Fig. 6b,7b). In the prediction, we obtained slight outward flows at centers of defects with large  $|\theta_0|$  (Fig. 4g, Extended Data Fig. 8a,b). By using ideal orientations and setting  $\pi'_0 = 0$  at central regions according to an assumption, the outward cellular vanished basically (Extended Data Fig. 9, Methods).

We finally propose a classification of dry active nematics based on our observed phenomena, given that our system cannot be categorized simply as contractile or extensile (as determined by the sign of  $\zeta$ ) due to the nonlinear active forces. Neglecting the gradients of  $\rho$  and  $S$  in equation (3), the direction of force along the radial direction is governed by the larger term between  $\pm\zeta$  and  $(\gamma_1 - \gamma_2)\rho S$ , where + (−) is for target (aster). When the nonlinear active forces dominate the linear terms ( $(\gamma_1 - \gamma_2)\rho S > \pm\zeta$ ), two new cases (region 2 and 4 in Fig. 4i) appear, in which both target and aster can be attractive or depleted. In our case, NPC monolayers are situated in the region 2, which has never been classified before.

### 3 Discussion

In this work, we explored the dynamics of NPC monolayers with +1 topological defects. Using shallow-ridged substrates to induce aster, spirals, and target, we observed cell accumulation near their center and inward cellular flow towards defect cores, regardless of the specific defect type. Analysis of experimental data, including orientations, velocities, and densities, revealed the origin of cellular flows across various defects, stressing the existence of the nonlinear active forces suggested by the hydrodynamic theory we derived from a relevant particle-level model. By incorporating these active forces, we quantitatively reproduced cellular flows in large-scale regions.

We believe that the accumulation phenomena described here are essentially due to generic properties of dense 2D cellular active nematics, despite some measurements of cell mounds at centers of defects being inaccurate. The chiral symmetry-breaking witnessed at various points along this work (Fig. 2f, Fig. 3f,h, Fig. 4h, Extended Data Fig. 2c) warrants further investigation, as it may be related to edge flow, shear flow, and cell sorting [29, 37–39]. Additionally, studying cell behaviors in monolayers featuring −1 topological defects is also an important direction for future research. Two nonlinear forces can produce outward flow for −1 defects, potentially leading to depletion at the center of these defects.

217 Our study fills a knowledge gap about how integer topological defects influence collective dynamics in 2D nematic  
218 cell sheets system. Defects of +1 topological charge provide aggregation sites, potentially influencing cell transport  
219 and morphogenesis in vivo [40]. Furthermore, the identification of emerging nonlinear active forces clarifies our under-  
220 standing of collective motion in active nematic systems, such as bacterial colonies, cytoskeletal filaments, colloids and  
221 3D morphogenesis [20, 22, 41–44]. We believe our study introduces a new way to quantify and classify cell sheets,  
222 highlights the influence of integer topological defects in the biomedical field, and could provide insights for controlling  
223 structure formation.

## 224 4 Methods

### 225 4.1 Cell culture

226 Mouse neural progenitor cells were originally from Ryoichiro Kageyama's lab, and mutants labelled by H2B-mCherry  
227 were made by Kyogo Kawaguchi. We used DMEM/F-12, HEPES, no phenol red (Thermo Fisher, 11039021) as medium  
228 base supplemented with basic fibroblast growth factor (bFGF) (20 ng/mL, Wako, 060-04543), epidermal growth factor  
229 (EGF) (20 ng/mL, Thermo Fisher, 53003-018) and N-2 Max (100x, R&D Systems, AR009). 35mm dishes were pre-  
230 coated with 10x diluted Matrigel (Corning, 356231) and medium (finally 30 $\mu$ L Matrigel in 1mL medium) overnight in  
231 37°C. Then we removed the coating agent and placed NPCs uniformly with 2mL medium. The initial cell density is  
232 around 5.5 \* 10<sup>-4</sup>/ $\mu$ m<sup>2</sup>. The cultures were incubated at 37°C with 5% CO<sub>2</sub> at saturated humidity. StemPro Accutase  
233 (Gibco, A1110501) was used to disassociate cells during passage progress, and Stem-Cellbanker (ZENOAQ, 11922)  
234 was applied for making frozen stocks.

### 235 4.2 PDMS substrate preparation

236 We designed the patterns in AutoCAD and produced the chromium mask accordingly, followed by lithography proce-  
237 dures. By spin-coating of SU-8 2002 (MicroChem) at 3000 rpm, we generated 1.2 $\mu$ m slots on the silicon wafer after  
238 lithography. PDMS liquid with a curing agent proportion of 1/8 (Dow Corning, Sylgard 184) was poured onto the  
239 silicon wafer and baked at 70°C for 3 hours. After solidification, we peeled the PDMS sheet off the silicon wafer and  
240 finally obtained a PDMS substrate with ridges. Given that the typical width of an elongated NPC is approximately  
241 10  $\mu$ m, in order to gently guide cells and not hinder their movement too much, we fabricated ridges of width 9 $\mu$ m  
242 and height 1.2 $\mu$ m, and set the distance between ridges to be in the range of 30 – 120 $\mu$ m. Multiple types of defects  
243 were integrated into a single PDMS sheet, facilitating simultaneous comparisons. Before seeding cells on the PDMS  
244 sheet, we applied plasma cleaner to improve hydrophilicity of the surface, sterilized it with 75% ethanol and UV for  
245 30 minutes separately, and washed using PBS and DMEM/F-12. In addition to the micropatterns presented in the  
246 main text, we also tested cell behavior on targets with  $R_{max}$  = 300, 600, 900 $\mu$ m. The consistent accumulation and  
247 the tendency of inward flow remained unchanged.

## 248 4.3 Imaging

249 For long time-lapse experiments, NPCs were plated onto Matrigel-coated PDMS substrates in glass base dishes (Iwaki).  
 250 NPCs were initially cultured in a  $CO_2$  incubator for two days until reaching the desired confluent density, after which  
 251 they were observed through phase contrast and fluorescent channels of a Leica DMi8 microscope. Tokaihit incubator,  
 252 which can maintain temperature and humidity and  $CO_2$  concentration, was assembled on the microscope to ensure  
 253 normal cell growth during recording. Double-channel images were captured every 6 minutes to reduce phototoxicity.  
 254 Steady integer topological defects induced by the guiding patterns could be observed over several days.

## 255 4.4 Nematic order

256 To characterize the local alignment of cells, we measured the orientational field from phase contrast images. Firstly,  
 257 we computed the gradient of the bright field  $I_{ij}$ , where  $ij$  indicated the positions of image pixels. This brightness  
 258 gradient was then smoothed using a Gaussian filter with a standard deviation of  $\sigma = 21\mu m$ . Subsequently, for each  
 259 pixel, we built the structure tensor [16, 45],

$$260 \quad H_{ij} = \begin{pmatrix} (\partial_x I_{ij})^2 & (\partial_x I_{ij})(\partial_y I_{ij}) \\ (\partial_x I_{ij})(\partial_y I_{ij}) & (\partial_y I_{ij})^2 \end{pmatrix} = \begin{pmatrix} H_{xx} & H_{xy} \\ H_{yx} & H_{yy} \end{pmatrix}. \quad (6)$$

261 The local orientation  $\theta_{ij}$  and coherency  $C_{ij}$  at each pixel was then determined using the formula:

$$262 \quad \theta_{ij} = \frac{1}{2} \arctan\left(\frac{2H_{xy}}{H_{xx} - H_{yy}}\right). \quad (7)$$

$$263 \quad C_{ij} = \frac{\sqrt{(H_{xx} - H_{yy})^2 + 4H_{xy}^2}}{H_{xx} + H_{yy}}. \quad (8)$$

264 In general, a coherency close to 1 means that the structure is locally 1D, a coherency close to 0 means that there is  
 265 no preferred direction. The nematic tensor order parameter  $Q_{ij}$  was calculated by

$$266 \quad Q_{ij} = \begin{pmatrix} \langle \cos(2\theta_{ij}) \rangle & \langle \sin(2\theta_{ij}) \rangle \\ \langle \sin(2\theta_{ij}) \rangle & \langle -\cos(2\theta_{ij}) \rangle \end{pmatrix} = \begin{pmatrix} Q_{xx} & Q_{xy} \\ Q_{yx} & Q_{yy} \end{pmatrix}, \quad (9)$$

267 where  $\langle \cdot \rangle$  represents a spatial average calculated using a 2D Gaussian filter with standard deviation  $\sigma = 42\mu m$ .  
 268 Scalar order parameter  $S$  is defined by  $\sqrt{Q_{xx}^2 + Q_{xy}^2}$ . The local spatial average orientational field  $\theta$  was obtained from  
 269  $\frac{1}{2} \arctan(Q_{xy}/Q_{xx})$ . For the ideal orientations,  $\theta_{ij} = \phi_{ij} + \theta_0$  in equation (9), ideal  $S$  is then obtained by the above  
 270 steps.

271 We also extracted orientation fields from cell nuclei in the fluorescent images. Briefly, we employed marker-controlled  
 272 watershed segmentation to detect the shapes of nuclei. Then we used ellipses to fit shapes and defined the long axis as  
 273 the orientation of single cell. See Supplementary Information (Section 2) for further detail. At last, these orientations  
 274 were averaged within a  $42 \mu\text{m}$  wide box to derive the local spatial average orientational fields.

#### 275 4.5 Cell velocity measurements

276 To obtain the cellular velocity, cell nuclei were tracked by TrackMate [46], a ImageJ plugin [47], in the fluorescent  
 277 images. The LoG detector and simple LAP tracking algorithm were employed. Prior to tracking, the images were  
 278 stabilized using the Image Stabilizer plugin in ImageJ. For  $i$ -th trajectory  $\mathbf{r}_i(t)$ , instantaneous velocity  $\mathbf{v}_i(t)$  was  
 279 estimated as the slope determined by  $\{\mathbf{r}_i(t-2), \mathbf{r}_i(t-1), \mathbf{r}_i(t), \mathbf{r}_i(t+1), \mathbf{r}_i(t+2)\}$ . The net velocity field  $\mathbf{v}(\mathbf{x}, \mathbf{y})$   
 280 was obtained by temporally and spatially vector averaging within a  $10 \mu\text{m}$  wide box, after which a 2D Gaussian filter  
 281 with standard deviation  $\sigma = 42 \mu\text{m}$  was applied.

282 To double-check the angle distributions of velocity fields, we also measured the cellular flows by applying an optical  
 283 flow algorithm on the fluorescent images. This algorithm is rooted in the Lucas–Kanade derivative of the Gaussian  
 284 method [48]. Spatial average was done with a  $42 \mu\text{m}$  wide box.

285 In the calculation of autocorrelation of the direction of instantaneous velocity,  $\langle \cos[\Delta\theta_{\mathbf{V}_0}(dt)] \rangle = \langle \cos[\theta_{\mathbf{V}_0}^i(t +$   
 286  $dt) - \theta_{\mathbf{V}_0}^i(t)] \rangle$ , where  $\mathbf{V}_0$  denotes instantaneous velocity,  $\theta_{\mathbf{V}_0}$  is the direction of  $\mathbf{V}_0$ ,  $i$  is the trajectory number,  
 287  $t \in [0, \text{duration of } i - \text{th trajectory}]$ ,  $dt$  is time interval ( $dt \in [0, \text{duration} - t]$ ), and  $\langle \cdot \rangle$  is the ensemble average over all  
 288 the trajectories ( $i$ ) and time ( $t$ ).  $\langle \cos[\Delta\theta_{\mathbf{V}_0}(dt)] \rangle$  over  $dt$  can be fitted with exponential  $\exp(-2dt/\tau_f)$ , where  $\tau_f$  is the  
 289 reversal time scale. In the Fig. 3c,  $k = -2/\tau_f$ .

#### 290 4.6 Cell density

291 For cell density quantification, we used the sum of fluorescent images after subtracting background. The background  
 292 of fluorescent signal was calculated as the average value of the lowest 0.02% of the total pixels. See Supplementary  
 293 Information (Section 3) for further detail about the transformations between fluorescent intensity and cell number.

#### 294 4.7 Estimation of parameters

295 For fitting, we normalized  $\rho$  by the mean density  $\rho_0$ . Then the equation (5) was transfromed into

$$296 (I - \epsilon' \rho' \mathbf{Q}) \rho' \mathbf{v} = -\zeta' \nabla \cdot \rho' \mathbf{Q} + \gamma_2' \rho' \mathbf{Q} \cdot (\nabla \cdot \rho' \mathbf{Q}) + \gamma_1' (\rho' \mathbf{Q} \cdot \nabla) \cdot \rho' \mathbf{Q} - \pi_0' \nabla \rho', \quad (10)$$

297 where  $\epsilon' = \rho_0 \epsilon$ ,  $\zeta' = \zeta / \gamma_0$ ,  $\gamma_2' = \gamma_2 \rho_0 / \gamma_0$ ,  $\gamma_1' = \gamma_1 \rho_0 / \gamma_0$ ,  $\pi_0' = \pi_0 / \gamma_0$ ,  $\rho' = \rho / \rho_0$ . For the convenience in writting, we set  
 298  $\mathbf{f}^{\text{friction}} = (I - \epsilon' \rho' \mathbf{Q}) \rho' \mathbf{v}$ ,  $\mathbf{f}^{a1} = -\nabla \cdot \rho' \mathbf{Q}$ ,  $\mathbf{f}^{a2} = \rho' \mathbf{Q} \cdot (\nabla \cdot \rho' \mathbf{Q})$ ,  $\mathbf{f}^{a3} = (\rho' \mathbf{Q} \cdot \nabla) \cdot \rho' \mathbf{Q}$ ,  $\mathbf{f}^{\text{diffusion}} = -\nabla \rho'$ . Then we

299 defined parameter vector  $\mathbf{P}$  and observation vector  $\mathbf{V}$

300 
$$\mathbf{P} = (\zeta', \gamma'_2, \gamma'_1, \pi'_0)^T, \quad (11)$$

301 
$$\mathbf{V} = (\mathbf{f}_{x1}^{\text{friction}}, \dots, \mathbf{f}_{xN}^{\text{friction}}, \mathbf{f}_{y1}^{\text{friction}}, \dots, \mathbf{f}_{yN}^{\text{friction}})^T, \quad (12)$$

302 where the subscript  $i = 1, 2, \dots, N$  denotes the observation at each grid point  $i$  of fields,  $N$  is the total number of the  
303 observation points,  $x, y$  denote components in cartesian coordinates. The input matrix  $\mathbf{X}$  is defined by

304 
$$\mathbf{X} = \begin{pmatrix} \mathbf{f}_{x1}^{a1} & \mathbf{f}_{x1}^{a2} & \mathbf{f}_{x1}^{a3} & \mathbf{f}_{x1}^{\text{diffusion}} \\ \vdots & \vdots & \vdots & \vdots \\ \mathbf{f}_{xN}^{a1} & \mathbf{f}_{xN}^{a2} & \mathbf{f}_{xN}^{a3} & \mathbf{f}_{xN}^{\text{diffusion}} \\ \mathbf{f}_{y1}^{a1} & \mathbf{f}_{y1}^{a2} & \mathbf{f}_{y1}^{a3} & \mathbf{f}_{y1}^{\text{diffusion}} \\ \vdots & \vdots & \vdots & \vdots \\ \mathbf{f}_{yN}^{a1} & \mathbf{f}_{yN}^{a2} & \mathbf{f}_{yN}^{a3} & \mathbf{f}_{yN}^{\text{diffusion}} \end{pmatrix}. \quad (13)$$

305 Then equation (9) can be written as  $\mathbf{V} = \mathbf{X}\mathbf{P}$ .

306 Given that both sides of the equation contain unknown parameters, we considered a fixed  $\epsilon'$  at first. We employed  
307 Bayesian inference method to keep the diffusion parameter  $\pi'_0$  positive [32, 49, 50]. This approach reformulated the  
308 equation into the problem of maximizing the posterior probability distribution function  $\Pi(\mathbf{P}|\mathbf{V})$  of the parameter set  
309 for the given  $\mathbf{V}$ :

310 
$$\Pi(\mathbf{P}|\mathbf{V}) = L(\mathbf{V}|\mathbf{P}) \times \pi(\mathbf{P}), \quad (14)$$

311 where the likelihood function  $L(\mathbf{V}|\mathbf{P})$  was defined as

312 
$$L(\mathbf{V}|\mathbf{P}) = \left( \frac{1}{\sqrt{2\pi\sigma^2}} \right)^{2N} \exp \left( -\frac{\|\mathbf{V} - \mathbf{X}\mathbf{P}\|^2}{2\sigma^2} \right), \quad (15)$$

313 and the prior distribution of the parameter set  $\pi(\mathbf{P})$  was defined as

314 
$$\pi(\mathbf{P}) = \left( \frac{1}{\sqrt{2\pi\sigma_0^2}} \right)^3 \exp \left( -\frac{\mathbf{P}_0^T \mathbf{P}_0}{2\sigma_0^2} \right) \times \left( \frac{1}{\sqrt{2\pi\sigma_{\pi_0}^2}} \right) \exp \left( -\frac{(\pi'_0 - \bar{\pi}_0)^2}{2\sigma_{\pi_0}^2} \right), \quad (16)$$

315 where the parameter vector was separated into two parts,  $\mathbf{P}_0 = (\zeta', \gamma'_2, \gamma'_1)^T$  and  $\pi'_0$ . Here, we set a positive bias ( $\bar{\pi}_0 > 0$ )  
316 to  $\pi'_0$  and assumed a Gaussian prior distribution. By maximizing the likelihood function, the optimal parameter set  
317 was obtained as

318 
$$\mathbf{P} = (\mathbf{X}^T \mathbf{X} + \Lambda I + (\Lambda_{\pi_0} - \Lambda) I')^{-1} (\mathbf{X}^T \mathbf{V} + \Lambda_{\pi_0} \bar{\pi}_0 J), \quad (17)$$

319 where  $\Lambda = \sigma^2/\sigma_0^2$ ,  $\Lambda_{\pi_0} = \sigma^2/\sigma_{\pi_0}^2$ ,  $I$  is the identity matrix,  $I'$  is a matrix in which only element  $I'(4, 4) = 1$  and all  
 320 other elements are 0,  $J = (0, 0, 0, 1)^T$ .  $\bar{\pi}_0$  was set by the estimation of the diffusion constant:  $\bar{\pi}_0 = v_0^2/\alpha$  where the  
 321 instantaneous velocity  $v_0 = 0.0067 \mu\text{m}/\text{s}$  and velocity reversal rate  $\alpha = 1/3600 \text{s}^{-1}$ . The initial values of  $\sigma^2$ ,  $\sigma_0^2$ ,  $\sigma_{\pi_0}^2$   
 322 were set as  $\sigma^2 = 10^{-6}(\mu\text{m}^2/\text{s}^2)$ ,  $\sigma_0^2 = 10^{-4}(\mu\text{m}^4/\text{s}^2)$ ,  $\sigma_{\pi_0}^2 = 10^{-4}(\mu\text{m}^4/\text{s}^2)$ . Using the calculated  $\mathbf{P}$ ,  $\sigma^2$  and  $\sigma_0^2$  were  
 323 updated by:

324

$$\sigma^2 = \frac{\|\mathbf{V} - \mathbf{X}\mathbf{P}\|^2}{2N}, \quad (18)$$

325

$$\sigma_0^2 = \frac{\mathbf{P}_0^T \mathbf{P}_0}{3}, \quad (19)$$

326 which were subsequently used to update  $\mathbf{P}$ . This cycle was iterated until the relative change of the  $\Lambda$  per iteration  
 327 became smaller than  $10^{-3}$ .

328 So far, with a fixed  $\epsilon'$ , we obtained the estimated parameters. Next, we varied  $\epsilon'$ , and for each  $\epsilon'$ , we used the  
 329 Bayesian method to obtain the estimated velocities as stated earlier. Then we calculated the determination coefficients  
 330 between the estimated velocities and the measured velocities. We selected the optimal  $\epsilon'$  and other parameters which  
 331 maximized the determination coefficients until the relative change of determination coefficients became smaller than  
 332  $10^{-5}$ .

## 333 4.8 Correction for the predicted outward flow of the center

334 Slight outward flows appear at centers of defects with large  $|\theta_0|$ , where the density is much higher (Fig. 4g, Extended  
 335 Data Fig. 8a,b). Here, we neglect the  $\nabla\rho$  term in equation (5) around centers ( $r < R_{min}$ ) according to an assumption  
 336 that cells can readily move to the third dimension and form cell mounds at high densities under compression. Addition-  
 337 ally, according to equation (3,4), active forces near centers are sensitive to the amplitude and gradient of  $S$  which we  
 338 could not reliably measure due to equipment limitations. By using ideal orientations ( $\theta = \theta_p$ ) and ideal  $S$  (Extended  
 339 Data Fig. 9b) according to the definition of defects and setting  $\pi'_0 = 0$  at regions with  $r < 80 \mu\text{m}$  (with other param-  
 340 eters as best-fit values), the outward cellular flows vanish basically (Extended Data Fig. 9a,c). This method causes  
 341 fluctuations in net velocity amplitudes around  $r = 80 \mu\text{m}$  (Extended Data Fig. 9a,c). To address this, we employ linear  
 342 interpolation to replace the fluctuating values (Extended Data Fig. 9e).

## 343 Code and data availability

344 All the codes and the data that support the findings of this study are available from the Z.Z. or M.S. upon request.

## 345 Supplementary information

346 Supplementary information is available in the online version of the paper.

## 347 Acknowledgements

348 We are grateful to Jacques Prost, Sriram Ramaswamy, Xiaqing Shi, Carles Blanch-Mercader, Aurelio Patelli, Eric  
349 Bertin, and Benoît Mahault for insightful discussions. We thank Kirsten D. Endresen for making micropatterns  
350 at the initial stage. M.S. acknowledges support from the Research Fund for International Scientists of NFSC  
351 (12174254,12250710131). H.Z. acknowledges support from NSFC (12225410 and 12074243).

## 352 Author contributions

353 M.S., F.S., H.Z., and Z.Z. conceived and designed the research. Z.Z., H.L., and Y.Y. performed the experiments. Z.Z.  
354 analyzed the experimental data. K.K. provided materials and tools. M.S., Y.Z., and H.C. developed the theoretical  
355 part. All the authors participated in writing and revising the manuscript.

## 356 Competing interests

357 The authors declare no competing interests.

## 358 References

- 359 [1] Kemkemer, R., Teichgräber, V., Schrank-Kaufmann, S., Kaufmann, D. & Gruler, H. Nematic order-disorder state  
360 transition in a liquid crystal analogue formed by oriented and migrating amoeboid cells. *The European Physical  
361 Journal E* **3**, 101–110 (2000).
- 362 [2] Doostmohammadi, A., Ignés-Mullol, J., Yeomans, J. M. & Sagués, F. Active nematics. *Nature Communications*  
363 **9**, 3246 (2018).
- 364 [3] Shankar, S., Souslov, A., Bowick, M. J., Marchetti, M. C. & Vitelli, V. Topological active matter. *Nature Reviews  
365 Physics* **4**, 380–398 (2022).
- 366 [4] Notbohm, J. *et al.* Cellular contraction and polarization drive collective cellular motion. *Biophysical Journal*  
367 **110**, 2729–2738 (2016).
- 368 [5] Saw, T. B., Xi, W., Ladoux, B. & Lim, C. T. Biological tissues as active nematic liquid crystals. *Advanced  
369 Materials* **30**, 1802579 (2018).
- 370 [6] Blanch-Mercader, C. *et al.* Turbulent dynamics of epithelial cell cultures. *Physical Review Letters* **120**, 208101  
371 (2018).
- 372 [7] Keber, F. C. *et al.* Topology and dynamics of active nematic vesicles. *Science* **345**, 1135–1139 (2014).

373 [8] Doostmohammadi, A., Thampi, S. P. & Yeomans, J. M. Defect-mediated morphologies in growing cell colonies.  
374 *Physical Review Letters* **117**, 048102 (2016).

375 [9] Duclos, G., Erlenkämper, C., Joanny, J.-F. & Silberzan, P. Topological defects in confined populations of spindle-  
376 shaped cells. *Nature Physics* **13**, 58–62 (2016).

377 [10] Sanchez, T., Chen, D. T., DeCamp, S. J., Heymann, M. & Dogic, Z. Spontaneous motion in hierarchically  
378 assembled active matter. *Nature* **491**, 431–4 (2012).

379 [11] Balasubramaniam, L. *et al.* Investigating the nature of active forces in tissues reveals how contractile cells can  
380 form extensile monolayers. *Nature materials* **20**, 1156–1166 (2021).

381 [12] Copenhagen, K., Alert, R., Wingreen, N. S. & Shaevitz, J. W. Topological defects promote layer formation in  
382 myxococcus xanthus colonies. *Nature Physics* **17**, 211–215 (2020).

383 [13] Giomi, L., Bowick, M. J., Ma, X. & Marchetti, M. C. Defect annihilation and proliferation in active nematics.  
384 *Physical Review Letters* **110**, 228101 (2013).

385 [14] Lavrentovich, T. T. *et al.* Topology control of human fibroblast cells monolayer by liquid crystal elastomer.  
386 *Science Advances* **6**, eaaz6485 (2020).

387 [15] De Gennes, P.-G. & Prost, J. *The Physics of Liquid Crystals* (Oxford university press, 1993).

388 [16] Kawaguchi, K., Kageyama, R. & Sano, M. Topological defects control collective dynamics in neural progenitor  
389 cell cultures. *Nature* **545**, 327–331 (2017).

390 [17] Saw, T. B. *et al.* Topological defects in epithelia govern cell death and extrusion. *Nature* **544**, 212–216 (2017).

391 [18] Ma, W. *et al.* Cell-extracellular matrix interactions regulate neural differentiation of human embryonic stem cells.  
392 *BMC developmental biology* **8**, 1–13 (2008).

393 [19] Gogola, A., Jan, N.-J., Lathrop, K. L. & Sigal, I. A. Radial and circumferential collagen fibers are a feature of the  
394 peripapillary sclera of human, monkey, pig, cow, goat, and sheep. *Investigative Ophthalmology & Visual Science*  
395 **59**, 4763–4774 (2018).

396 [20] Hamant, O. *et al.* Developmental patterning by mechanical signals in arabidopsis. *Science* **322**, 1650–1655 (2008).

397 [21] Provenzano, P. P. *et al.* Collagen reorganization at the tumor-stromal interface facilitates local invasion. *BMC*  
398 *Medicine* **4**, 1–15 (2006).

399 [22] Maroudas-Sacks, Y. *et al.* Topological defects in the nematic order of actin fibres as organization centres of hydra  
400 morphogenesis. *Nature Physics* **17**, 251–259 (2020).

401 [23] Guillamat, P., Blanch-Mercader, C., Pernollet, G., Kruse, K. & Roux, A. Integer topological defects organize  
402 stresses driving tissue morphogenesis. *Nature Materials* **21**, 588–597 (2022).

403 [24] Endresen, K. D., Kim, M., Pittman, M., Chen, Y. & Serra, F. Topological defects of integer charge in cell  
404 monolayers. *Soft Matter* **17**, 5878–5887 (2021).

405 [25] Kaiyrbekov, K. *et al.* Migration and division in cell monolayers on substrates with topological defects. *Proceedings  
406 of the National Academy of Sciences* **120**, e2301197120 (2023).

407 [26] Zhao, Z. *et al.* (2024). Submitted.

408 [27] Selinger, J. V. *Introduction to the Theory of Soft Matter: From Ideal Gases to Liquid Crystals* (Springer, 2016).

409 [28] Li, H., Zhao, Z., Zhao, Y., Yao, Y. & Sano, M. (2024). To be published.

410 [29] Yamauchi, L., Hayata, T., Uwamichi, M., Ozawa, T. & Kawaguchi, K. Chirality-driven edge flow and non-  
411 Hermitian topology in active nematic cells (2020). Preprint at <https://arxiv.org/abs/2008.10852>.

412 [30] Ramaswamy, S. Active matter. *Journal of Statistical Mechanics: Theory and Experiment* **2017**, 054002 (2017).

413 [31] Toner, J., Tu, Y. & Ramaswamy, S. Hydrodynamics and phases of flocks. *Annals of Physics* **318**, 170–244 (2005).

414 [32] Uwamichi, M. *et al.* Experimental identification of force, velocity, and nematic order relationships in active  
415 nematic cell monolayers (2024). Preprint at <https://arxiv.org/abs/2402.16151>.

416 [33] Patelli, A., Djafer-Cherif, I., Aranson, I. S., Bertin, E. & Chaté, H. Understanding dense active nematics from  
417 microscopic models. *Physical Review Letters* **123**, 258001 (2019).

418 [34] Bertin, E. *et al.* Mesoscopic theory for fluctuating active nematics. *New Journal of Physics* **15**, 085032 (2013).

419 [35] Peshkov, A., Bertin, E., Ginelli, F. & Chaté, H. Boltzmann-ginzburg-landau approach for continuous descriptions  
420 of generic vicsek-like models. *The European Physical Journal Special Topics* **223**, 1315–1344 (2014).

421 [36] Maitra, A. *et al.* A nonequilibrium force can stabilize 2d active nematics. *Proceedings of the National Academy  
422 of Sciences* **115**, 6934–6939 (2018).

423 [37] Mijalkov, M. & Volpe, G. Sorting of chiral microswimmers. *Soft Matter* **9**, 6376–6381 (2013).

424 [38] Yashunsky, V. *et al.* Chiral edge current in nematic cell monolayers. *Physical Review X* **12**, 041017 (2022).

425 [39] Duclos, G. *et al.* Spontaneous shear flow in confined cellular nematics. *Nature Physics* **14**, 728–732 (2018).

426 [40] Alvarez-Buylla, C. L., García-Verdugo, J.-M. & Arturo. Chain migration of neuronal precursors. *Science* **271**,  
427 978–981 (1996).

428 [41] Basaran, M., Yaman, Y. I., Yuce, T. C., Vetter, R. & Kocabas, A. Large-scale orientational order in bacterial  
429 colonies during inward growth. *Elife* **11**, e72187 (2022).

430 [42] Zhang, R. *et al.* Spatiotemporal control of liquid crystal structure and dynamics through activity patterning.  
431 *Nature Materials* **20**, 875–882 (2021).

432 [43] Schaller, V., Weber, C., Semmrich, C., Frey, E. & Bausch, A. R. Polar patterns of driven filaments. *Nature* **467**,  
433 73–77 (2010).

434 [44] Liu, Z. T. *et al.* Activity waves and freestanding vortices in populations of subcritical quincke rollers. *Proceedings  
435 of the National Academy of Sciences* **118**, e2104724118 (2021).

436 [45] Jähne, B. *Spatio-temporal Image Processing: Theory and Scientific Applications* (Springer, 1993).

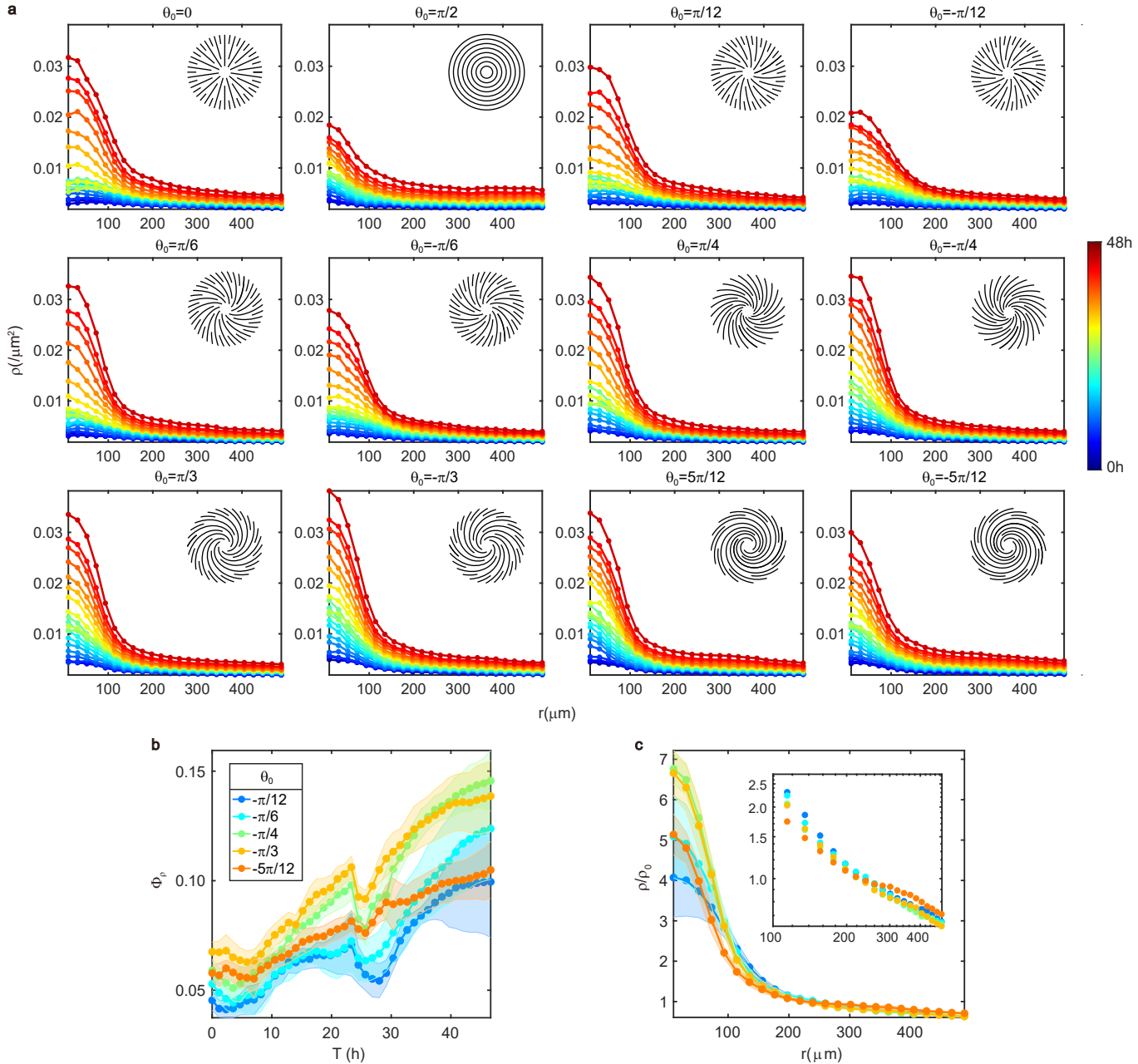
437 [46] Tinevez, J.-Y. *et al.* Trackmate: An open and extensible platform for single-particle tracking. *Methods* **115**, 80–90  
438 (2017).

439 [47] Abràmoff, M. D., Magalhães, P. J. & Ram, S. J. Image processing with imagej. *Biophotonics International* **11**,  
440 36–42 (2004).

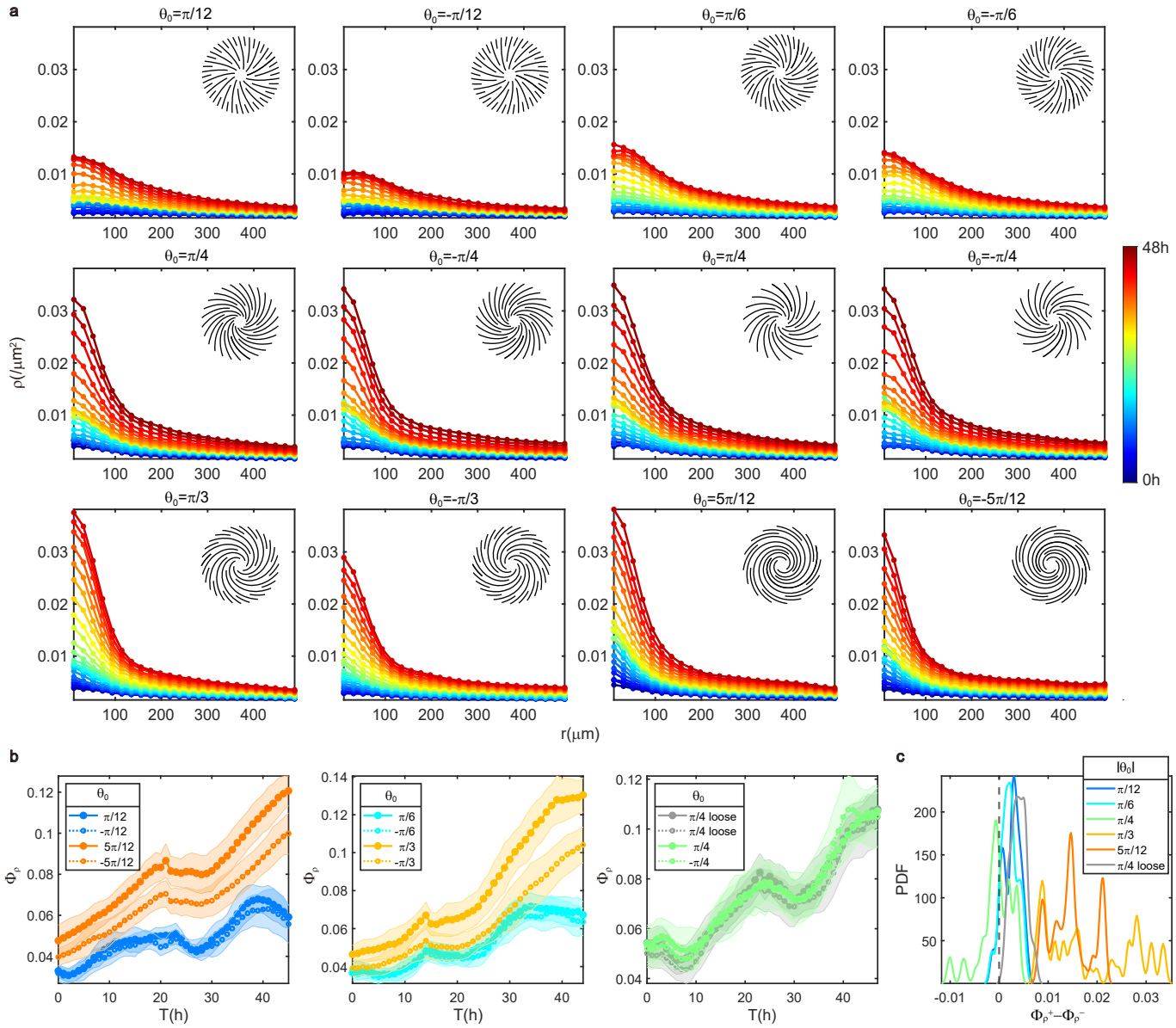
441 [48] Lucas, B. D. & Kanade, T. Hayes, P. J. (ed.) *An iterative image registration technique with an application to  
442 stereo vision.* (ed.Hayes, P. J.) *IJCAI'81: 7th international joint conference on Artificial intelligence*, Vol. 2,  
443 674–679 (William Kaufmann, Vancouver, Canada, 1981).

444 [49] Ishihara, S. & Sugimura, K. Bayesian inference of force dynamics during morphogenesis. *Journal of Theoretical  
445 Biology* **313**, 201–211 (2012).

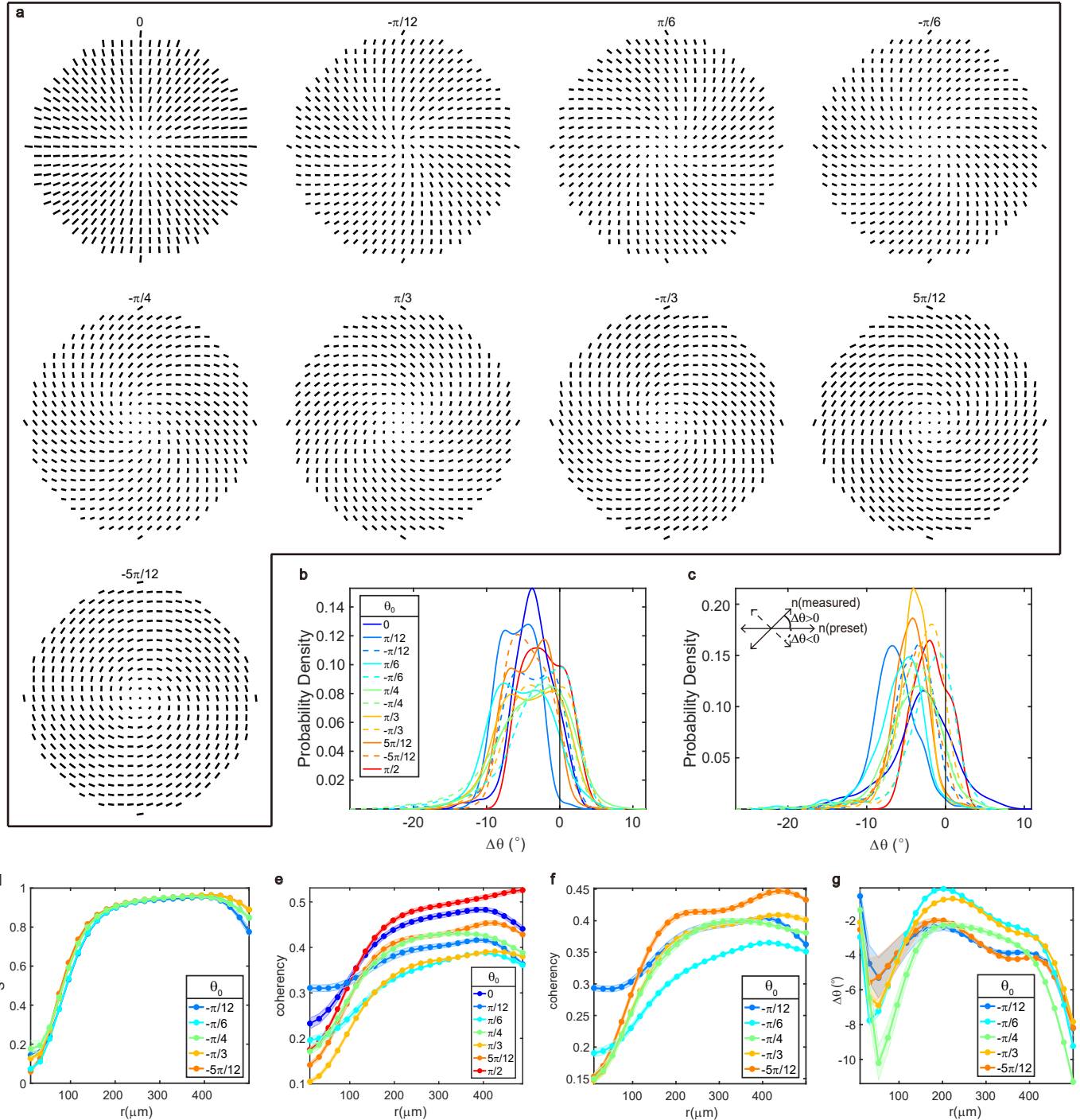
446 [50] von Toussaint, U. Bayesian inference in physics. *Reviews of Modern Physics* **83**, 943–999 (2011).



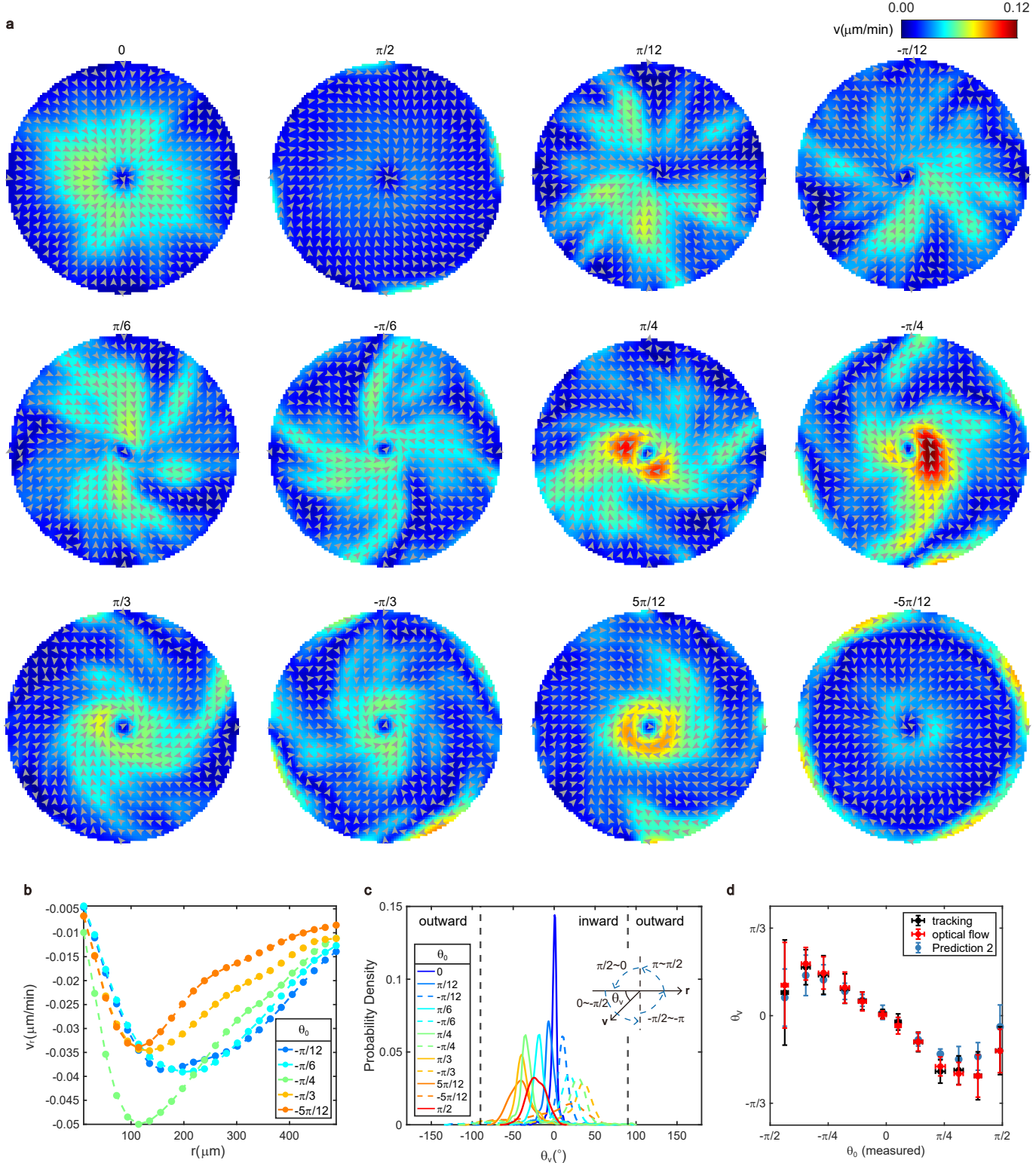
**Extended Data Fig. 1** Cell density evolution of all defects which are arranged on one PDMS sheet. **a**, Time evolution of cell density distributions. Density profiles are obtained by taking the average of data captured every 1 hour, and the color encodes time lapse. **b**, Average percentage of cells  $\Phi_\rho$  ( $\Phi_\rho = n(r < R_{min})/n(r < R_{max})$ , where  $n$  is the cell number) assemblies with time on defects with negative  $\theta_0$ . Colors of curves depict different defects. **c**, Normalized radial density profiles by mean density  $\rho_0$  when  $\rho_0 = 0.009/\mu\text{m}^2$ . Inset: A log-log plot for the region with  $r > 100\mu\text{m}$ . Legend in **b**. N of each type of defects is 6.



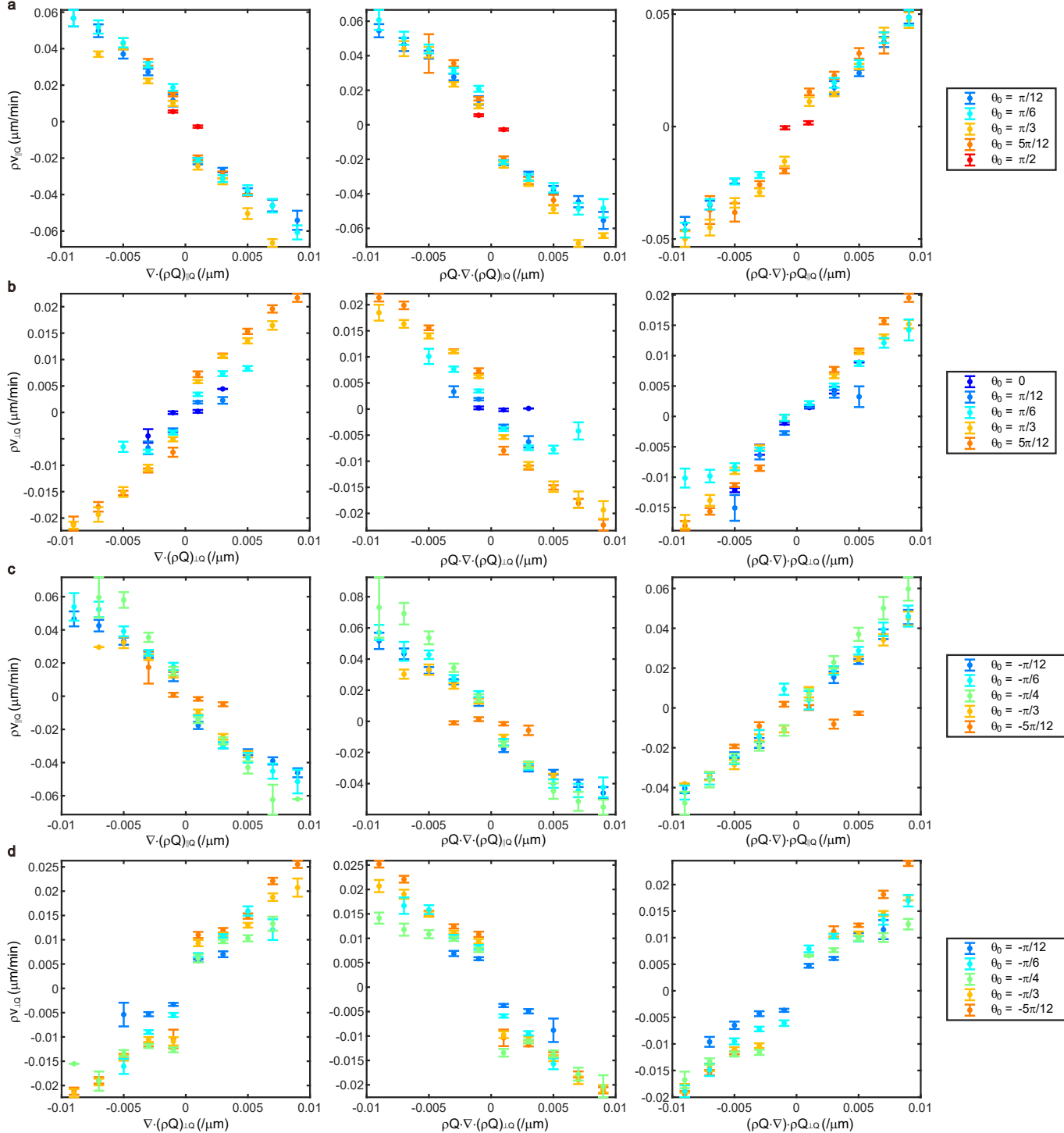
**Extended Data Fig. 2** NPCs accumulate at the center of spirals and show more prominent accumulation on counterclockwise spirals compared with clockwise spirals. **a**, Time evolution of cell density distributions on spirals. Density profiles are obtained by taking average of data captured every 1 hour, and the color encodes time lapse. Defects with  $\theta_0 = \pm\pi/12, \pm 5\pi/12$  are on one PDMS sheet, so are the defects with  $\theta_0 = \pm\pi/6, \pm\pi/3$ , and the defects with  $\theta_0 = \pm\pi/4, \pm\pi/4$  (looser confinements). N of each type of spirals is 16. **b**, Average percentage of cells  $\Phi_\rho$  ( $\Phi_\rho = n(r < R_{min})/n(r < R_{max})$ , where n is the cell number) assemblies with time on defects with negative  $\theta_0$  and on patterns with looser confinements. Colors of curves depict different defects. **c**, Distribution of the difference between  $\Phi_\rho$  of clockwise spirals and counterclockwise spirals. The difference is calculated every 1 hour for defects with opposite sign but the same absolute value of  $\theta_0$ . In **b** and **c**, data are presented as mean  $\pm$  s.d.



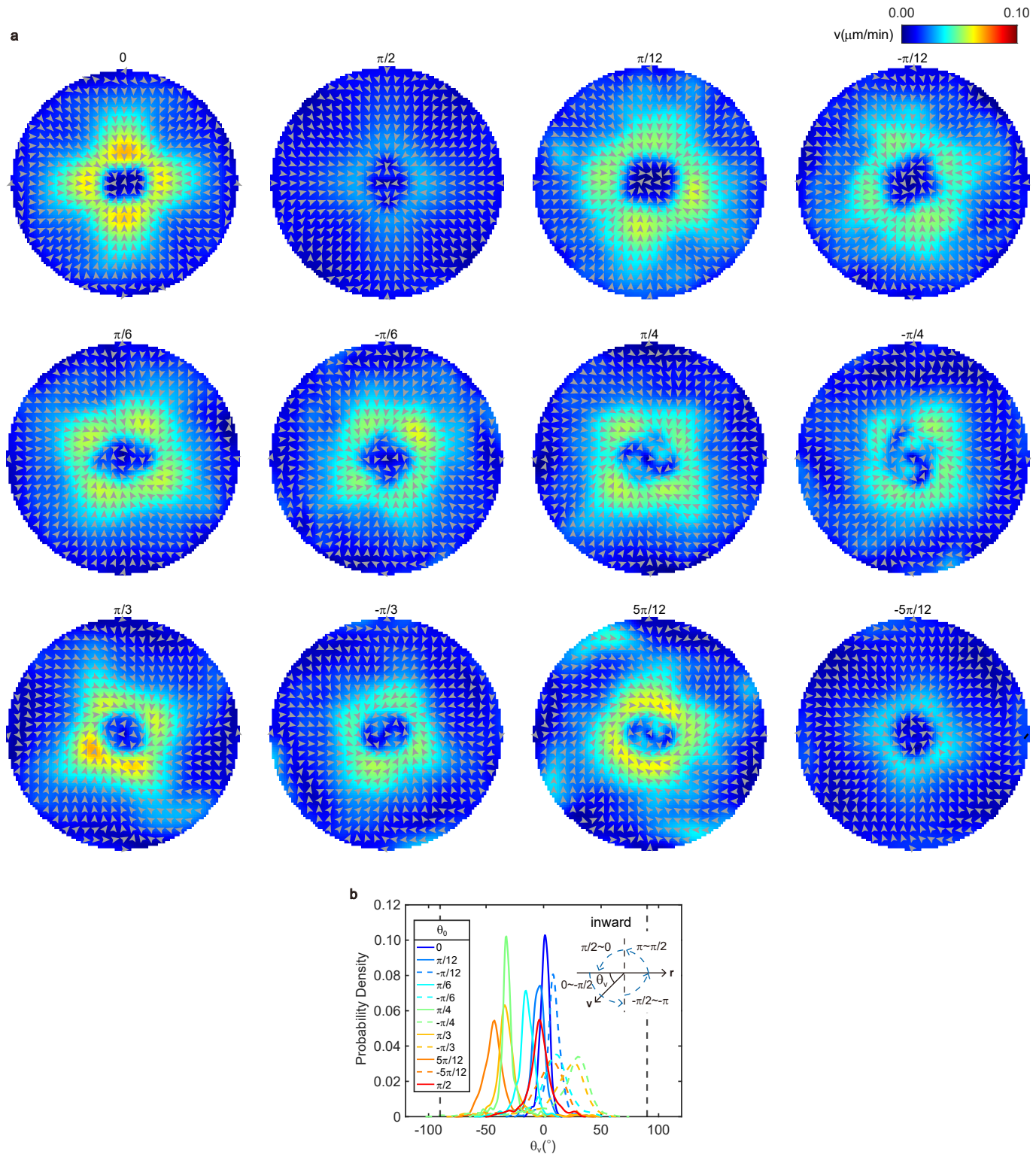
**Extended Data Fig. 3** Orientational analysis on aster, spirals, and target. **a**, Measured orientational fields by structure tensor method. The length of line corresponds to the coherency. Titles are values of  $\theta_0$ . **b**, Probability density function of the angle ( $\Delta\theta$ ) between the experimentally measured cell orientation by structure tensor method and orientation preset by PDMS pattern. **c**, Probability density function of the angle ( $\Delta\theta$ ) between the experimentally measured cell orientation by detecting single cell and orientation preset by PDMS pattern. Inset shows the definition of  $\Delta\theta$ . Legend in **b**,  $r < 100 \mu\text{m}$  was excluded. **d**, Radial profiles of order parameter  $S$  for clockwise spirals. **e**, Radial profiles of coherency for aster, counterclockwise spirals and target. **f**, Same as **d** but for coherency. **g**, Same as **d** but for  $\Delta\theta$  detected by structure tensor method. In **d**, **g**, data are presented as mean  $\pm$  s.d., and s.d. are calculated from different times. In **e**, **f**, data are presented as mean  $\pm$  s.e.m., and s.e.m. are calculated from different times. In **a** – **g**, data are averaged by 32 asters (10h), 16 spirals for each type (10h) and 32 targets (10h).



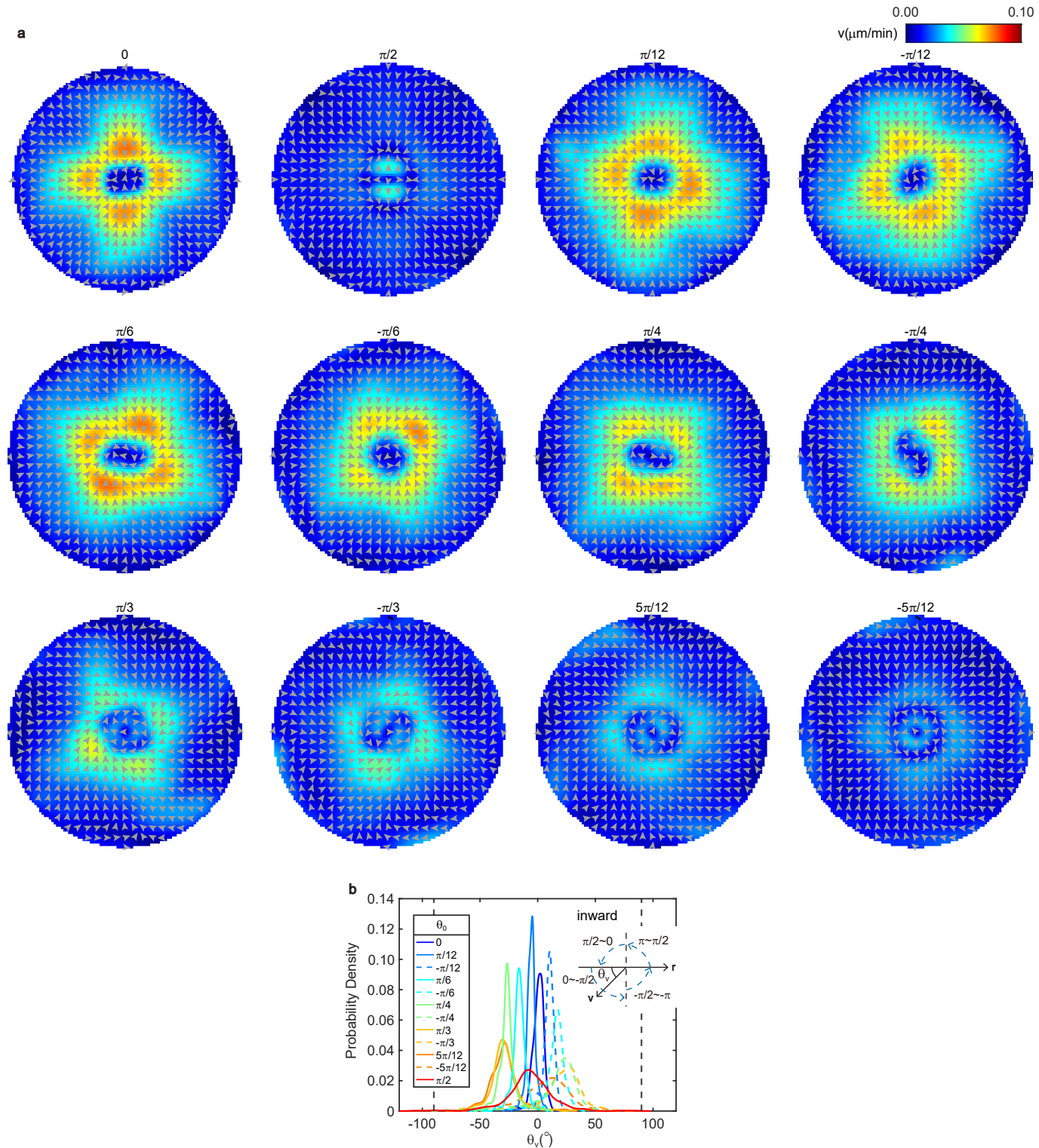
**Extended Data Fig. 4** Net velocity fields on aster, spirals, and target. **a**, Net velocity fields calculated from tracking results across all the defects. Colors depict the amplitude of net velocity. Titles are values of  $\theta_0$ . **b**, Radial profiles of the net radial velocity for clockwise spirals. **c**, Probability density function of the angle ( $\theta_v$ ) between net velocity and inward radial direction on all types of defects. Velocity fields are calculated from optical flow method. Insets show the definition of  $\theta_v$ . Regions with  $r < 100\mu\text{m}$  are excluded. **d**, Measured and predicted  $\theta_v$  versus measured  $\theta_0$ . Black dots are the same experimental data as those in Fig. 2i.  $\theta_v$  of red dots are obtained from the location of peaks in c. Prediction 2 comes from method (ii). In **a**–**d**, data are averaged by 32 asters (10h), 16 spirals for each type (10h) and 32 targets (10h).



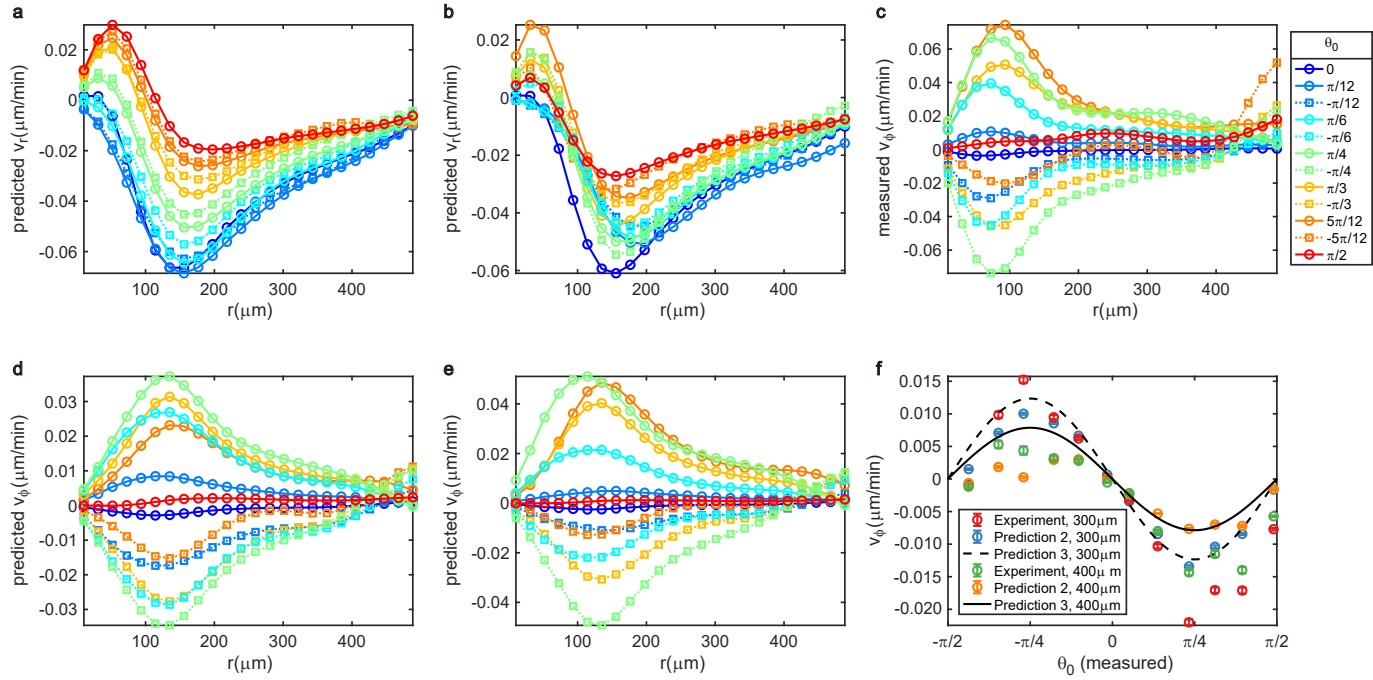
**Extended Data Fig. 5** The comparison between components of cellular flow  $\rho v$  and components of active forces.  $\parallel \mathbf{Q}$  ( $\perp \mathbf{Q}$ ) is defined as the component parallel (perpendicular) to the principal axis of  $\mathbf{Q}$ . **a**, Comparisons between parallel components for defects with positive  $\theta_0$ . **b**, Comparisons between perpendicular components for the aster and spirals with positive  $\theta_0$ . **c**, Comparisons between parallel components for spirals with negative  $\theta_0$ . **d**, Comparisons between perpendicular components for spirals with negative  $\theta_0$ . Data are presented as mean  $\pm$  s.e.m.

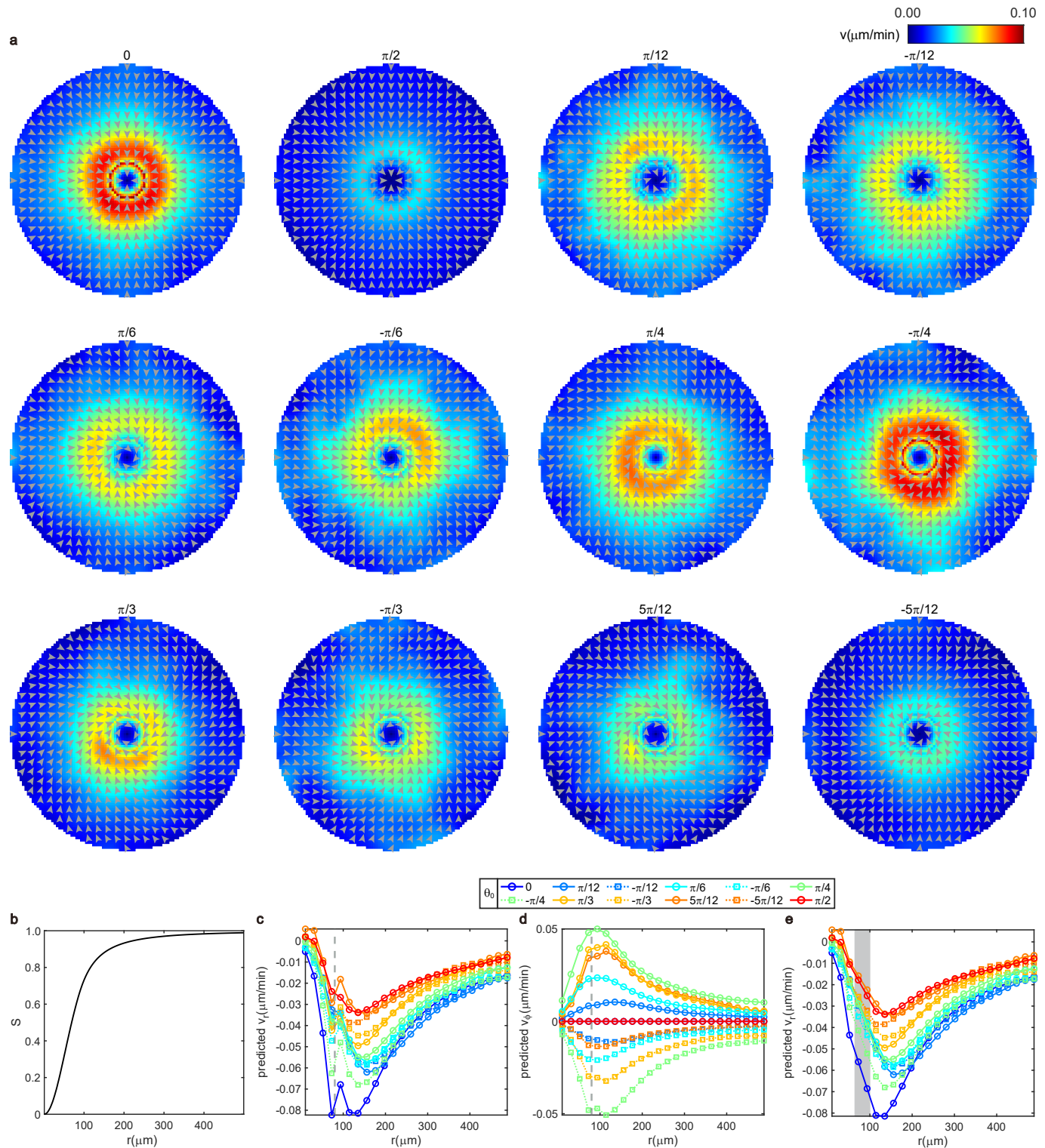


**Extended Data Fig. 6** Predicted velocities by best-fit parameters on aster, spirals, and target. **a**, Predicted net velocity fields across all the defects. Colors depict the amplitude of net velocity. Titles are values of  $\theta_0$ . **b**, Probability density function of the angle ( $\theta_v$ ) between predicted net velocities and inward radial direction on all types of defects. Insets show the definition of  $\theta_v$ . The prediction method is method (i). Regions with  $r < 100\mu\text{m}$  are excluded.



**Extended Data Fig. 7** Predicted velocities by average parameters on aster, spirals, and target. **a**, Predicted net velocity fields across all the defects. Colors depict the amplitude of net velocity. Titles are values of  $\theta_0$ . **b**, Probability density function of the angle ( $\theta_v$ ) between predicted net velocities and inward radial direction on all types of defects. Insets show the definition of  $\theta_v$ . The prediction method is method (ii). Regions with  $r < 100\mu\text{m}$  are excluded.





**Extended Data Fig. 9** Correction for the predicted outward flow of the center. **a**, Predicted velocities by best-fit parameters and perfect orientations according to the definition of integer topological defects on aster, spirals, and target. In regions with  $r < 80\mu\text{m}$ ,  $\pi'_0 = 0$ . Titles are values of  $\theta_0$ . **b**, Radial profiles of order parameter  $S$  on the ideal integer topological defects. **c**, **d**, **e**, Radial profiles of the predicted radial velocities (**c**), and azimuthal velocities (**d**). In regions with  $r < 80\mu\text{m}$  (Left part of the dashed line in **c**, **d**),  $\pi'_0 = 0$ . In **e**, we use linear interpolation to reduce fluctuations around  $r = 80\mu\text{m}$  (gray region).

**Extended Data Table 1** Best-fit parameters and determinate coefficients ( $R^2$ ) for each kind of pattern.

$\theta_0$	Parameters					$R^2$
	$\zeta'(\mu m^2/s)$	$\gamma'_2(\mu m^2/s)$	$\gamma'_1(\mu m^2/s)$	$\pi'_0(\mu m^2/s)$	$\epsilon'$	
$-5\pi/12$	0.0197	-0.0457	0.0316	0.0403	0.1300	0.8224
$-\pi/3$	0.0264	-0.0379	0.0498	0.0689	0.1900	0.8371
$-\pi/4$	0.0375	-0.0327	0.0648	0.1041	0.2200	0.8519
$-\pi/6$	0.0268	-0.0208	0.0724	0.1166	0.0210	0.8284
$-\pi/12$	0.0164	-0.0079	0.0656	0.0991	0.2000	0.8756
0	0.0275	-0.0152	0.0535	0.0594	0.1500	0.9551
$\pi/12$	0.0151	-0.0043	0.0758	0.0994	0.1800	0.8876
$\pi/6$	0.0296	-0.0069	0.0679	0.0820	0.0580	0.8740
$\pi/4$	0.0590	-0.0230	0.0557	0.0512	0.0200	0.8915
$\pi/3$	0.0321	-0.0296	0.0507	0.0503	0.2010	0.9060
$5\pi/12$	0.0434	-0.0508	0.0579	0.0862	0.3110	0.8928
$\pi/2$	0.0289	-0.0257	0.0564	0.0732	0.1476	0.8173